ELECTROKINETICALLY ACTIVE NANOWELLS

A Dissertation

Presented to the Faculty of the Graduate School

of Cornell University

In Partial Fulfillment of the Requirements for the Degree of

Doctor of Philosophy

by

Bernardo Cordovez

January 2011

ELECTROKINETICALLY ACTIVE NANOWELLS

Bernardo Cordovez, Ph. D.

Cornell University 2011

In this research I developed a new form of microfluidic transport technique that exploits electrokinetic phenomena in discrete micro and nanometer sized wells. Through the use of these “Electroactive Nanowells”, I have been able to demonstrate the reversible trapping of micro and nanoscale objects in discrete locations, enabled a new form of microfluidic memory and used a modified version of this technique to generate a wireless drug delivery system for the control of flying insects.

The outcome of this research is threefold: First, it establishes a low power device that can increase the speed of traditional microwell screening techniques by four orders of magnitude in an easy to fabricate setup. The second outcome is the development of the first high density microfluidic memory, which can store up to 6 bits of material storage in single 200 nanometer wells; providing a 6 order magnitude increase in storage density over traditional microfluidic storage devices. Third, I exploited the essential transport physics of this approach to enable a wireless and implantable drug delivery system capable of dispensing various chemicals on demand; and applied it to the of chemically directed control of live micro air vehicles. Fourth, I present a flexible version of this drug delivery system by using only polymers in the fabrication process.

BIOGRAPHICAL SKETCH

Bernardo Cordovez was born in 1983 in Quito, Ecuador. After graduating from Colegio Americano de Quito, Ecuador in 2001, he joined the University of California at Santa Barbara where he received a Bachelor of Science in Mechanical Engineering with Distinction in the Major. Bernardo then joined Prof. David Erickson's "Integrated Micro- and Nanofluidic Systems Laboratory" as the first graduate student in his research group. He was awarded a Master of Science in Mechanical Engineering in August 2008. Following graduation, he will continue his career as a Postdoctoral Associate under Prof. Erickson.

To my grandfather, el Dr. Santos. R.I.P.

ACKNOWLEDGMENTS

First I would like to thank my advisor Dr. Erickson. I met David when he was still a post doctoral researcher at the California Institute of Technology. David was the first person who truly believed in my potential as an effective researcher. Under his guidance, I have received advice in and beyond my field of study, and he is a leading example of how combining innovation with dedication and hard work can lead to great results. David brought me to Cornell, and because of that I am forever in debt with him. My graduate experience at Cornell has been the most rewarding time of my life and it is all due to him.

I would like to acknowledge my graduate committee: Dr. Edwin C. Kan and Dr. Antje Baeumner of Cornell University. I appreciate all of their support and insight throughout this process.

I would also like to thank all of the members of the "Integrated Micro- and Nanofluidic Systems Laboratory". Particularly Aram J. Chung, my friend and colleague in the Insect Cyborgs project from whom I've learned a tremendous amount and is probably the kindest person I know (along with my mom). I would also like to thank Mekala Krishnan and Sudeep Mandal, both of which are great friends and tremendous colleagues who have helped me solve complex problems; even we never worked on the same projects. Finally, I would like to thank the people that worked under my guidance, particularly Nipun Jasuja and Suraj Kabadi, who undoubtedly have tremendous futures ahead of them.

I would like to thank my colleagues and friends in Cornell University's Mechanical and Aerospace Engineering graduate program, notably Edgar Cuji, Vishal Tandon, Justin Atchison, Alex Barbati, Michael Kalontarov, Juan Salazar and Mike Tolley, for always being there for me. I value their friendship and camaraderie and hopefully will

see them beyond December of 2010. Justin in particular was of great help towards the end of my Ph. D, and I cannot thank him enough.

I would also like to thank Marcia Sawyer, Cornell University's Mechanical and Aerospace Engineering Graduate Field Administrator. Marcia is solely responsible for keeping the department together, managing egos from both young and less young, always with a constant smile in her face.

Last but not least, to my family. My uncle Rodrigo, who believed in me from the get-go, and sponsored and mentored me through my undergraduate career, and needless to say I arrived to Cornell thanks to him. My mom Laura, who is nothing short of awesome and the most supportive person in this planet. My dad Santiago, the first person I knew who was really interested in science, and who is intrigued with Cornell as the place of my graduate study, as well as that of Carl Sagan's tenure. My brother Juan Diego, who told me that I should study something more interesting and novel than the internal combustion engine (an electrical engineer at his finest), and the first person who introduced me to nanotechnology. My sister, Maria, a great person to talk to when in need, hope to see her soon in Europe when all of this is done!

Finally, to my girlfriend Maria. She has put up with me through thick and thin over the last 3 years. Te quiero Senorita!

TABLE OF CONTENTS

Biographical Sketch iii
Dedication iv
Acknowledgements v
Table of Contents vii
List of Figures viii
List of Tables ix
List of Symbols x
Chapter 1. Introduction 1
Chapter 2. Trapping and Storage of Particles in Electroactive Microwells 21
Chapter 3. Electroactive Micro and Nanowells for Optofluidic Storage 34
Chapter 4. Hybrid Chemical-Electric Control Over Flying Bio-Robotic Systems 62
Chapter 5. A Flexible and Multiplexed Polymer Drug Delivery System 78
Chapter 6. Conclusions 96

LIST OF FIGURES

Figure 2.1 Electroactive Microwells 24
Figure 2.2 Time Lapse of Particle Attraction and Repulsion in a 20 μm Well 26
Figure 2.3 Finite Element Analysis of Electrokinetic Effects in 20 μm Well 29
Figure 3.1 Optofluidic Storage of Quantum Dots 38
Figure 3.2 Electroactive Nanowells 39
Figure 3.3 Spectrographic Readout and Mean Fluorescent Excitation 42
Figure 3.4 Large Electroactive Microwell 44
Figure 3.5 Attraction Time Scales vs. Mean Channel Velocity 45
Figure 3.6 Non-volatile Storage Device Schematic 48
Figure 3.7 Mean Fluorescent Excitation History in an Electroactive Microwell 50
Figure 3.8 Fluorescent Signal Retention History in a Gel Coated Microwell 51
Figure 3.9 Spectrographic Readout for Well Shown in Figure 3.4 53
Figure 3.10 Mean Fluorescent Intensity vs. Time Trace for Electroactive Microwell 53
Figure 3.11 SEM of the Cross Section of the Electroactive Microwell Geometry 54
Figure 3.12 Homogeneous Data Packet Separated Into RGB constituents 54
Figure 4.1 Hybrid Chemo-Electrical Control Schematic and Layout 67
Figure 4.2 Hybrid Chemo-Electrical Control Operation 68
Figure 4.3 Locomotive Activity Recovery 70
Figure 4.4 Flight Endurance Enhancement via Electrical Stimuli 71
Figure 5.1 Device Layout and Assembly 81
Figure 5.2 Electrochemical Ejection Procedure 83
Figure 5.3 Device Ejection Volumetric Performance Results at 30V 84
Figure 5.4 Fluidic Channel Multiplexing 85
Figure 5.5 Cell Viability as a Function of Substrate and Time 86
Figure 5.6 Biocompatibility of Polyimide and Silicon Needles 87

LIST OF TABLES

Table 3.1 Time Scale Summary of Microwell Traps 48

LIST OF SYMBOLS

ρ	=	mass density
U	=	pressure driven fluid velocity
v	=	particle velocity
L_e	=	characteristic length
η	=	dynamic viscosity
Re	=	Reynolds number
Q	=	flow rate
R_a	=	pipe radius
P	=	pressure
ρ_E	=	volumetric charge density
E	=	electrical field
c	=	ion concentration
z_i	=	valence
F	=	Faraday's constant
R	=	gas constant
T	=	temperature
ϕ	=	electric potential
λ_D	=	Debye length
I_c	=	ionic stength
ε	=	permittivity of the medium
ζ	=	surface (zeta) potential
S	=	trapping stability parameter
q	=	electric charge of particle
k_b	=	Boltzmann's constant

v_{EO} = electroosmotic velocity

μ_{EO} = electroosmotic mobility

v_{EP} = electrophoretic velocity

μ_{EP} = electroophoretic mobility

v_{DEP} = dielectrophoretic velocity

μ_{DEP} = dielectrophoretic mobility

CHAPTER 1

INTRODUCTION

1.1 Research Scope

In this research I developed a new form of microfluidic transport technique that exploits electrokinetic phenomena in confined micrometer and nanometer scale wells. Through the use of these "Electroactive Nanowells", I have been able to demonstrate the reversible trapping of micro and nanoscale objects in discrete locations, enabled a new form of microfluidic memory and used this confined electrokinetic phenomena for on command drug delivery in vitro as well as in living insects.

The first contribution from this research is the ability to enhance the temporal performance of traditional microwell screening systems [1, 2] by four orders of magnitude in a low power and easy to fabricate device. My second contribution is the development of a microfluidic memory that can store up to 6 bits of material storage in single 200 nanometer data sites, providing a six order magnitude increase in storage density over traditional microfluidic storage devices [3] and the potential to generate the next generation in high memory density bioinformatic devices. Third, I exploited the essential transport physics of this approach to enable a wireless and implantable drug delivery system capable of dispensing various chemicals on demand, and applied it to the chemically directed control of flying bio-robotic systems.

In the remainder of this chapter, I present a brief introduction to microfluidics: Why this field is important and what are its current limitations, and most importantly how my research brings about new solutions for these limitations as well as new frontiers for this field. I then present my accomplishments in Chapters 2 through

Chapter 5 and conclude my findings and present future directions for my work in Chapter 6.

1.2 Micro and Nanofluidics: Motivation

As the name states, microfluidics studies fluid flows in the micro and nanometer scales, and this field became immediately popular in an array of fields due to fundamental engineering advantages it provides in these spatial dimensions. For biomolecule screening research [4-6] for example, the sensing volumes are reduced to the same scale order as that of target [7] and thus enable high detection sensitivity [8] with trace amounts of analyte. This favorable engineering scaling extends beyond the life sciences. The cavitation force that enables inkjet printing **[ref gmail]**, for example [9] is only possible since small droplet masses can be launched at accelerations up to 70,000 times that of gravity [10] for an infinitesimal applied macro scale force (~100μN) as dictated by Newton's Second law.

The small size of microfluidic devices also allows for portable and non invasive health monitoring systems like the modern glucose sensor [11]. This field plays significant role in other point-of-care diagnostic devices [12, 13], like in the female pregnancy and male fertility tests, and even in assays that screen for cardiac [14] and pathogenic bio-markers [15]. Microfluidic applications are also advantageous from an economic standpoint since these devices can use small amounts of expensive and sometimes difficult to isolate analyte, or even provide fast and cheap avenues for amplifying it [16] when necessary. Like its silicon microchip counterpart, this field also benefits from advancements in microfabrication as dictated by Moore's Law, and has even contributed new fabrication paradigms [17] that make even cheaper mass production of these devices possible.

All the advantages listed above have contributed to the generation of cheap and high throughput detections systems with multiple screening sites; the most popular of these being DNA [1] and cell microarrays [2]. Unfortunately, there are two main drawbacks in the operation of current microfluidic devices: the first is due to transport limitations associated with downscaling, and the second is related to device integration and packaging as will be shown below.

1.3 Challenges

The first and most important challenge I faced in my work is fundamental and ubiquitous in all nanoscale fluidic devices: There are fluidic transport limitations associated with downscaling.

1.3.1: Fluid Transport in the Small Scales

Fluid flow in small scales (particularly the nanoscale) has generally been viewed as a fundamental grid lock in fluid mechanics as opposed to a place for opportunity. As is well established in classical fluid mechanics, the Reynolds number, *Re*, which is a non-dimensional measure of the ratio of inertial and viscous forces, is determined by:

$$Re = \rho U L_e / \eta \tag{1.1}$$

Where ρ *is* the mass density, U is the fluid velocity, L_e is the characteristic length and η is the dynamic viscosity. This parameter is usually very small in the small scales, where flows are subject to well defined but sluggish streams that do not mix easily. If we are to look at traditional pressure driven (pipe) flow to drive microfluidic transport in a circular pipe, we find that the flow-rate Q scales as:

$$Q = (-\pi R_a^4/8\eta)\ (\partial P/\partial z) \quad (1.2)$$

Where R_a is the pipe radius, P the forcing pressure term and z marks the longitudinal direction. As evidenced by this equation, pressure driven flow-rate scales with the hydraulic diameter to the fourth power and thus flow-rate diminishes abruptly when channel dimensions are reduced to the nanoscale [18].

Fortunately, micro and nanoscale fluid mechanics is unique in that there are many unique transport mechanisms that can generate and enhance fluid flows in ways that are simply not possible in the macro scale. In my work, the transport mechanisms I exploit for flow in the micro and nanoscale are referred to as electrokinetic effects [19]. The relevant electrokinetic effects will be described in the key concepts section in this chapter, but for now it suffices to say that electrokinetic flows scale more favorably in sub micrometer dimensions than pressure driven flow, with the flow rate of electroosmotic flow scaling with the with R_a^2 [18] (just the area of the channel) instead of R^4 as dictated by pressure driven flow.

The first half of my work as a graduate student was devoted to identifying the appropriate combination of pressure driven and electrokinetic transport mechanisms for electoactive microwell trapping to maximize the device speed and performance, with the aim of significantly reducing the sample collection time for traditional microwell and microfluidic memory devices.

1.3.2: Device Integration

The ability to integrate microfluidic systems with existing medical and electronic devices as well as difficulties in packaging is by many regarded as the main reason why microfluidic devices have experienced somewhat limited adoption for commercial applications [20]. As such, building from one of the most widely used

biomolecule screening templates is very important since it is well received by researchers. I believe my work in electroactive wells can generate an impact in the field due to its two most important qualities: It enhances the temporal performance of traditional passive screening systems [1], [2] by offering a quicker and reversible trapping capability mentioned above; and second, these wells offer a high degree of application dependent reconfigurability. By having a common denominator device that can be easily modified to perform various applications, I ventured electroactive wells into the fields of microfluidic storage and in drug delivery for flying insect locomotive control as will be expanded in Section 1.4 below.

1.4 Microfluidic Applications Enabled Through My Work

1.4.1: High Density Microfluidic Memories

Less than 50 years ago, many scientists still stipulated that fluidic and pneumatic memories could compete with their electronic counterparts. The pure fluidic amplifier [21] for example, could modulate fluidic flows for toggling between two memory states much like a transistor uses electric current for the same purpose. While the battle in terms of memory storage and speed was quickly lost due to the great speed, low cost and advancements in large scale integration offered by electronics, fluids have the capability of transporting physical matter in the form of chemistry and biology. As such, microfluidic memories aim at integrating chemistry and biology with computation through the use of small scale fluidic elements [3], [22], [23].

There are two important limitations of current microfluidic memories. The first one is that to date, fluidic memory storage density borders 50Bits/cm^2 [3], which is between 8 and 9 orders of magnitude smaller than current commercial single layer

optical and electronic storage media. To elucidate the reader the immense gap in storage density between the aforementioned fluidic techniques versus electronic and magnetic storage, I present a quick glance at the state of the art in electromagnetic media. To start, perpendicular magnetic storage [24] where the poles in magnetic subdomains are perpendicularly aligned to the recording surface, enabling a high storage density of 65 GBits/cm². "Racetrack" storage [25] developed by IBM® has also raised much research interest. This technique enables multiple bit storage in nanowires organized in 3D [26] by exploiting the spin coherent current. Also highest measured storage density in a research environment has been made available by holographic quantum encoding [27], where the researchers showed the ability to read 35bits/electron (or nearly $5*10^8$ Gbyte/cm^2). In the far field optics realm, optical holographic data storage [28] which works on reading and writing data based on optical beam interference patterns shows the most promise with recorded densities up to 75 GBits/cm². For a more more elaborate description the state of the optical storage devices is presented in Section 3.2. Though here there was an emphasis on density, it is important to note that read/writing speed, performance and repeatability are the most important factors for commercial adoption of these techniques. Equally important, as mentioned above, is that microfluidics offers the necessary access to analyze small amounts of chemistry and biology. So while microfluidic memories are not to compete directly with electronic and magnetic storage media, there is still a significant amount of research that needs to be done which focuses on increasing and enabling the amount of analytical operations performed in microfluidic systems, which becomes a big issue when nanoscale matter is to be analyzed.

The second limitation is that the slow speed of traditional microfluidic devices makes them not feasible for commercial adoption. I addressed both problems by devising 200nm sized electrokinetic wells capable of fast and reversible trapping of

semiconductor nanoparticles (Quantum Dots) in these confined locations. Furthermore, by exploiting the fact that the light emission properties of these particles can be tuned with their size [29], this research aims at detecting different combinations of these particles in single diffraction limited data sites in order to enable a multiple bit microfluidic device.

1.4.2: Chemical Control Over Flying Bio-Robotic Systems

Micro Air Vehicles are a subset of Unmanned Aircraft which have raised a lot of research interest for surveillance and remote sensing applications [30]. Almost the entirety of unmanned aircraft control systems is made up of electronic and mechanical components that guide the aircraft and control its maneuverability. However, as the aircraft's dimensions are reduced, two coupled fundamental problems arise. The first is related the fluid scaling described above: Small aircraft have small airfoils and as such a low Reynolds number [31]. This means that since fluid mixing isn't very effective in millimeter and sub-millimeter scales for slow flying vehicles, the aerodynamics become heavily compromised since flow separation occurs more favorably in laminar streams and as such and maneuverability becomes very challenging. The second issue is power consumption. To first order, energy storage is volumetric, and as such small systems will have a lower energy capacity. Furthermore, small robotic flying systems [32] are traditionally power hungry (precisely because aerodynamics are compromised at the small scales) and like any aircraft, they need to provide enough power to lift both the main body and battery weight.

Nature on the other hand, has already solved two of these fundamental problems through flying insects. Even in their small size, insects can achieve strong lift through their elaborate wing flapping motion which helps them maximize their aerodynamic

efficiency. Furthermore, insects undergo an important nourishing stage during metamorphosis. In the case of the insects used in this research, namely Manduca Sexta moths, they feed throughout their pupal stage for a period of approximately 18 days before their cuticle is released (ecdysis); making it possible for them to fly for miles while carrying payloads of 1 gram in addition to their body weight. The challenge then becomes fusing active functionality to these living systems to enable on command control of maneuverability. Most of the work performed to date on live micro-air vehicle control approaches this challenge using only electric stimulation [33-35] since electricity offers a high degree of pulsed based neuromuscular control. Recently, my colleague Aram J. Chung showed that chemical payloads can be delivered via implantable microfluidic devices to change the metabolism and reduce the locomotive activity of these moths during tethered flight [36]. In this section of my work, I integrated his recently established microfluidic control with the established electrical control techniques to generate a hybrid approach for live micro air manipulation, and aim to show that these two approaches are synergistic and can pave the way towards a fully integrated micro air vehicle. The implantable drug delivery device was devised through a modified version of my electroactive wells, and also gave it wireless functionality to deliver chemical agents to a moth during untethered flight.

1.5 Key Concepts and Background Theory

In order to provide a clear picture to the reader, I provide a quick overview of a few important and common transport phenomena mentioned throughout this dissertation:

1.5.1: The Electrical Double Layer

One of the most important aspects about microfluidic devices in general is that the spatial dimensions and geometries are such that they have a very large surface area to volume ratios. Here I explore a very important electrochemical interface for microfluidics (and interface science in general) known as the Gouy-Chapman electrical double layer. [18]

If a charged surface comes into contact with an ionic solution (like buffered water), ions oppositely charged to surface (counterions) will feel a coulombic attraction force towards it, and these ions will stack on the surface forming a region that experiences a net electrical charge known as the Electrical Double Layer. The way these counterions stack is adequately modeled using Poisson-Boltzmann statistics, yielding:

$$c_i = c_{i,\infty} exp(-z_i F \phi / RT) \tag{1.3}$$

where c_i is the concentration of ion species at a given potential (which actually maps with the distance from the wall as dictated from the wall), $c_{i,\infty}$ is the concentration of that species in the bulk fluid (far from the wall), z_i is the electric valence of the species, ϕ is the electric potential (ϕ =0 far from the wall), F is the Faraday constant, T temperature and R is the gas constant. We can now look at the electrostatic body force term

$$\rho_E = \sum_i c_i z_i F \tag{1.4}$$

which when inserted back to Eqn. 1.3 yields

$$\rho_E = \sum_i c_{i,\infty} z_i F exp(-z_i F \phi / RT) \tag{1.5}$$

Eqn. 1.5 links the local electrostatic potential, ionic concentration and charge density. To obtain the governing equation, we first invoke the Poisson equation:

$$\nabla^2 \phi = \rho_E / \varepsilon \tag{1.6}$$

Where ε is the permittivity of the fluid medium, to obtain

$$\nabla^2 \phi = (-F/\varepsilon) \sum_i c_{i,\infty} z_i exp(-z_i F \phi / RT) \tag{1.7}$$

Since these gradients evidence that the spatial distribution of potential is very important, we can obtain the characteristic length scale, or Debye length:

$$\lambda_D = (\varepsilon RT/2F^2 I_c)^{1/2} \quad (1.8)$$

where I_c represents the ionic strength of the solution, given by

$$I_c = (1/2)\sum_i c_i z_i^2 \quad (1.9)$$

The ionic strength then plays a key role in determining how far the Debye length extends from the surface. For low ionic strengths, λ_D extends very far from the surface, up to 1 μm with deionized water. At higher ionic concentrations the double layer is said to be shielded by ions and is smaller in size, and scales with the inverse square root.

In the electroactive microwell and nanowell systems that I will explore, slat concentration plays a very important role in the trapping processes.

1.5.2: Electrokinetics

Now that the electrochemical interactions are better understood, we now look at how they couple to fluid mechanics. Since most microfluidic applications are under Stokes flow conditions ($Re << 1$), the governing Navier-Stokes equations take following form [31] under the influence of a forcing electrostatic body force $\rho_E E$.

$$\nabla P - \eta \nabla^2 v = \rho_E E \quad (1.5)$$

Here ρ_E is the volumetric charge density and E is the forcing external electrical field. Electrokinetic flows take shapes and forms in an array of different coupling mechanisms [37-40]. Below I describe the two most relevant to my work.

1.5.2a: Electro-Osmosis

When a charged surface (or surface that becomes charged due to deprotonation) comes in contact with a liquid, the ions oppositely charged to the surface will be

drawn towards it and form a nanoscale region with a net charge known as the Electrical Double Layer [41]. The potential drop that occurs between the bulk fluid (far away from the surface) and across the Electric Double Layer is known as the Zeta Potential (ζ). When an extrinsic electric field is applied longitudinally in a fluidic channel, the diffuse ions in the Double layer with charge counter to the surface will be drawn to the oppositely charged side of the channel. Given the viscous nature of the flow at the small scales, the ions will push the adjacent fluid sheets until a uniform "plug" flow type profile is formed. The velocity of this flow, v_{EO} can be described by the Helmholtz-Smoluchowsky relationship:

$$v_{EO} = -\varepsilon\zeta E/\eta \tag{1.4}$$

Where ε is the permittivity of the fluid medium, ζ is the potential drop from the wall to the bulk and E is the forcing electrical field term. The term $\varepsilon\zeta E/\eta$ is lumped into a factor describe as the electro-osmotic mobility, which is the scaling between the fluid flow and the forcing electrical field.

1.5.2b: Electrophoresis

Though phenomenologically very similar to electroosmosis, it can be understood as the transport a charged particle experiences under an applied electric field while subjected to fluid drag [18]. This particle transport can be described as the electro-osmotic condition for a channel that goes from $R= \infty$ to $R=$ r with a scaling factor f [18] that accounts for the size mismatch between the Debye length and particle size. Because of this scaling, electrophoresis is particularly useful in DNA and RNA separation techniques [38, 42]. Like electro-osmosis, electrophoretic transport is easily reversible by switching the polarity of the applied field, which is a tool I frequently used in the first half of my research.

One key aspect to note is that most traditional electro-osmotic and electrophoretic systems have very high power requirements. The reason for that is that one must apply

a very large voltage (usually in the tens of KV [43]) in order to generate sizeable electric fields over millimeter to centimeter long distances; such as the ones necessary for traditional electroosmotic transport across microfluidic channels.

We now focus a little more on electrostatics. Here we find that for a given electric potential, the electric field scales with the voltage gradient. From a linear circuits standpoint, conservation of current (Kirchoff's law) indicates that resistance scales linearly with a resistor's axial length and inversely with its cross-sectional area, thus the voltage drop will mainly occur in regions of high resistance. Moreover, since the electric field E follows the relationship [44]:

$$E = -\nabla\phi \tag{1.5}$$

Where ϕ is the electric potential, one can achieve high electric field concentrations in very narrow and tall geometries (high aspect ratio), which is precisely the basis of my micro and nanowells and the fundamental engineering scaling advantage my work provides.

1.5.3: Electrolysis of Water:

Electrolysis of water results is the decomposition of liquid water into its gas constituents through an oxidation/reduction reaction driven by DC potentials in excess of 1.23V [45]. Electric current is necessary to drive this reaction because this phase change will not occur spontaneously at standard temperature and pressure. Generally, electrolysis is used in industrial processes to isolate hydrogen, but is generally avoided in physiological experiments since electrolysis will change the local pH and ion concentration of microenvironments and potentially tamper with biology. Because of this fact, most of the micro and nanowell experiments were operated below this threshold voltage.

However, I also show in my work that one can actually exploit water electrolysis to generate efficient microfluidic pumps for drug delivery applications by paying careful attention to device design and geometry. I used this pumping mechanism to deliver chemicals on demand to flying insects in mid air and paralyze their wing flapping activity. It should be noted beforehand that severe use of electrolysis can actually clog the fluidic dispensing with gas bubbles as will be elaborated in Chapter 5, however it is the primary pumping mechanism for these drug delivery devices. In the next section I will present the breakdown of my research and the organizational framework of this dissertation.

1.6 Research Overview and Dissertation Breakdown

Chapter 2 is the first demonstration of a working electroactive microwell system and the most important stepping stone in my graduate work. Here I demonstrated strong, fast and reversible trapping of small micro particles subjected to a pressure driven flow into electroactive microwells through a combination of the electrokinetic effects explained in Section 1.5. The fundamental advantage of the system is that it enables high trapping potentials due to the spatial confinement of the well geometry. Furthermore, the device was easily fabricated in a single layer process and since it is packaged in a traditional microwell architecture like the ones used in Proteomic, Cell and DNA microarrays, it can be easily integrated with these systems to provide active trapping functionality instead of relying on their traditionally slow, indiscriminate and irreversible transport processes.

Chapter 3 overviews how my work on nanofluidics can pave the way for integrating physical matter and data storage for next generation bioinformatic systems. By pushing the limits of nanofabrication, I developed electroactive nanowells with the

same diameter as a Blu-Ray® data bumps which are capable of reversibly trapping and detecting semiconductor nanocrystals (~15nm in diameter) through a new version of the device presented in Chapter 2. The semiconductor nanocrystals were spectrally encoded, and I was able to independently distinguish up to 6 encoded bits in a single diffraction limited nanowell, making it possible to obtain a geometric increase in storage density over current single layer optical storage devices, and up to 7 orders of magnitude higher than existing fluidic memories. This chapter also explores the possibility of using micrometer sized wells for nanocrystal display devices, and presents the use of an agarose gel matrix that helps sustain long term storage of the trapped semiconductor nanocrystals (and thus enhance signal retention) without having to rely on an external power source.

Chapter 4 shifts gears, and focuses on the role of microfluidic devices for controlling the flight behavior of flying bio-robotic systems. As explained in Section 1.4.2, microfluidics devices offer new possibilities for these systems including the potential of mid flight nourishing and chemically induced flight retardation without recurring to strong electrical signals that may cause irreparable damage to moth's physiology. With the help of my colleague Aram J. Chung, we demonstrated an implantable microfluidic device which uses as its drug delivery system a pressure building electrochemical reaction and the electrokinetic ejection procedure of Electoractive Microwells. The implanted microneedle was used to eject an L-Glutamic acid neurotransmitter solution into a Manduca Sexta moth's thorax, which elevates neuron membrane potential until the insect's nervous system is over-excited, ultimately resulting in a reversible, chemically induced mid flight paralysis. Simultaneously, an additional electrode setup was used to provide on command electrical stimuli which prompted the cyborg moth to take off from rest, and also enhanced flight activity in mid air. Furthermore, we demonstrated that the chemical

signal are strong enough to override electrical stimulation, and also presented avenues for enhancing a moth's flight endurance while tracking its displacement using an indoor GPS system.

Chapter 5 presents a next generation version of the active microfluidic drug delivery needles presented in Chapter 4. In this work, I shifted from the hard and brittle silicon based drug delivery architecture to an all polymer microfluidic system composed of soft acrylic and polyimide, capable of localized and timed drug delivery which is not easily achieved with traditional diffusion governed drug delivery devices. Flexibility is essential for implantable drug delivery systems if they are not to shatter during insertion or the tissue re-adaptation phase. Furthermore, this new version has multiple individually addressable fluidic reservoirs capable of controlled dispensing of different chemicals and doses as required. Its performance was comparable to that of previously established silicon based drug delivery systems, and I concluded this chapter with an assessment of its biocompatibility, showing that it is more easily accepted by mammalian cells than its silicon predecessor.

Chapter 6 concludes the work presented by summarizing my research contributions to microfludics, and highlights future directions that could arise from my work.

REFERENCES

1. Schena, M., D. Shalon, R.W. Davis, and P.O. Brown, *Quantitative Monitoring of Gene Expression Patterns with a Complementary DNA Microarray.* Science, 1995. **270**(5235): p. 467-470.
2. Rettig, J.R. and A. Folch, *Large-scale single-cell trapping and imaging using microwell arrays.* Analytical Chemistry, 2005. **77**(17): p. 5628-5634.
3. Thorsen, T., S.J. Maerkl, and S.R. Quake, *Microfluidic large-scale integration.* Science, 2002. **298**(5593): p. 580-584.
4. Bowden, M., L.N. Song, and D.R. Walt, *Development of a microfluidic platform with an optical imaging microarray capable of attomolar target DNA detection.* Analytical Chemistry, 2005. **77**(17): p. 5583-5588.
5. Zaytseva, N.V., R.A. Montagna, and A.J. Baeumner, *Microfluidic biosensor for the serotype-specific detection of Dengue virus RNA.* Analytical Chemistry, 2005. **77**(23): p. 7520-7527.
6. Zheng, B., L.S. Roach, and R.F. Ismagilov, *Screening of protein crystallization conditions on a microfluidic chip using nanoliter-size droplets.* Journal of the American Chemical Society, 2003. **125**(37): p. 11170-11171.
7. Erickson, D., S. Mandal, A.H.J. Yang, and B. Cordovez, *Nanobiosensors: optofluidic, electrical and mechanical approaches to biomolecular detection at the nanoscale.* Microfluidics and Nanofluidics, 2008. **4**(1-2): p. 33-52.
8. Dawson, E.D., C.L. Moore, J.A. Smagala, D.M. Dankbar, M. Mehlmann, M.B. Townsend, et al., *MChip: A tool for influenza surveillance.* Analytical Chemistry, 2006. **78**(22): p. 7610-7615.

9. de Gans, B.J., P.C. Duineveld, and U.S. Schubert, *Inkjet printing of polymers: State of the art and future developments.* Advanced Materials, 2004. **16**(3): p. 203-213.

10. Meinhart, C.D. and H.S. Zhang, *The flow structure inside a microfabricated inkjet printhead.* Journal of Microelectromechanical Systems, 2000. **9**(1): p. 67-75.

11. Mastrototaro, J., *The MiniMed Continuous Glucose Monitoring System (CGMS).* Journal of Pediatric Endocrinology & Metabolism, 1999. **12**: p. 751-758.

12. Yager, P., T. Edwards, E. Fu, K. Helton, K. Nelson, M.R. Tam, and B.H. Weigl, *Microfluidic diagnostic technologies for global public health.* Nature, 2006. **442**(7101): p. 412-418.

13. Herr, A.E., A.V. Hatch, D.J. Throckmorton, H.M. Tran, J.S. Brennan, W.V. Giannobile, and A.K. Singh, *Microfluidic immunoassays as rapid saliva-based clinical diagnostics.* Proceedings of the National Academy of Sciences of the United States of America, 2007. **104**(13): p. 5268-5273.

14. Kurita, R., Y. Yokota, Y. Sato, F. Mizutani, and O. Niwa, *On-chip enzyme immunoassay of a cardiac marker using a microfluidic device combined with a portable surface plasmon resonance system.* Analytical Chemistry, 2006. **78**(15): p. 5525-5531.

15. Zaytseva, N.V., V.N. Goral, R.A. Montagna, and A.J. Baeumner, *Development of a microfluidic biosensor module for pathogen detection.* Lab on a Chip, 2005. **5**(8): p. 805-811.

16. Khandurina, J., T.E. McKnight, S.C. Jacobson, L.C. Waters, R.S. Foote, and J.M. Ramsey, *Integrated system for rapid PCR-based DNA analysis in microfluidic devices.* Analytical Chemistry, 2000. **72**(13): p. 2995-3000.

17. Anderson, J.R., D.T. Chiu, R.J. Jackman, O. Cherniavskaya, J.C. McDonald, H.K. Wu, S.H. Whitesides, and G.M. Whitesides, *Fabrication of topologically complex three-dimensional microfluidic systems in PDMS by rapid prototyping.* Analytical Chemistry, 2000. **72**(14): p. 3158-3164.

18. Kirby, B., *Micro- and nanoscale fluid mechanics: Transport in microfluidic devices*. 2010: Cambridge University Press. 358.

19. Ramos, A., H. Morgan, N.G. Green, and A. Castellanos, *Ac electrokinetics: a review of forces in microelectrode structures.* Journal of Physics D-Applied Physics, 1998. **31**(18): p. 2338-2353.

20. Blow, N., *Microfluidics: the great divide.* Nat Meth, 2009. **6**(9): p. 683-686.

21. Dellert, R.C., *Fluidic Logic Design.* Instruments & Control Systems, 1969. **42**(6): p. 138-&.

22. Groisman, A., M. Enzelberger, and S.R. Quake, *Microfluidic memory and control devices.* Science, 2003. **300**(5621): p. 955-958.

23. Prakash, M. and N. Gershenfeld, *Microfluidic bubble logic.* Science, 2007. **315**(5813): p. 832-835.

24. Iwasaki, S.I., *Perpendicular magnetic recording-Its development and realization.* Proceedings of the Japan Academy Series B-Physical and Biological Sciences, 2009. **85**(2): p. 37-54.

25. Parkin, S.S.P., M. Hayashi, and L. Thomas, *Magnetic Domain-Wall Racetrack Memory.* Science, 2008. **320**(5873): p. 190-194.

26. Thomas, L., M. Hayashi, X. Jiang, R. Moriya, C. Rettner, and S. Parkin, *Resonant Amplification of Magnetic Domain-Wall Motion by a Train of Current Pulses.* Science, 2007. **315**(5818): p. 1553-1556.

27. Moon, C.R., L.S. Mattos, B.K. Foster, G. Zeltzer, and H.C. Manoharan, *Quantum holographic encoding in a two-dimensional electron gas.* Nature Nanotechnology, 2009. **4**(3): p. 167-172.

28. Coufal, H.J., D. Psaltis, and G. Sincerbox, *Holographic Data Storage*. Springer Series in Optical Sciences. Vol. 76. 2000: Springer-Verlag.

29. Alivisatos, A.P., *Semiconductor clusters, nanocrystals, and quantum dots.* Science, 1996. **271**(5251): p. 933-937.

30. Shyy, W., M. Berg, and D. Ljungqvist, *Flapping and flexible wings for biological and micro air vehicles.* Progress in Aerospace Sciences, 1999. **35**(5): p. 455-505.

31. White, F.M., *Fluid Mechanics*. 6 ed. 2008: McGraw Hill. 247.

32. Wood, R.J., *The first takeoff of a biologically inspired at-scale robotic insect.* Ieee Transactions on Robotics, 2008. **24**(2): p. 341-347.

33. Bozkurt, A., R.F. Gilmour, and A. Lal, *Balloon-Assisted Flight of Radio-Controlled Insect Biobots.* Ieee Transactions on Biomedical Engineering, 2009. **56**(9): p. 2304-2307.

34. Sato, H., C.W. Berry, Y. Peeri, E. Baghoomian, B.E. Casey, G. Lavella, J.M. Vandenbrooks, J.F. Harrison, and M.M. Maharbiz, *Remote radio control of insect flight.* Front Integr Neurosci, 2009. **3**: p. 24.

35. Tsang, W.M., A.L. Stone, Z.N. Aldworth, J.G. Hildebrand, T.L. Daniel, A.I. Akinwande, and J. Voldman, *Flexible Split-Ring Electrode for Insect Flight Biasing Using Multisite Neural Stimulation.* Ieee Transactions on Biomedical Engineering, 2010. **57**(7): p. 1757-1764.

36. Chung, A.J. and D. Erickson, *Engineering insect flight metabolics using immature stage implanted microfluidics.* Lab on a Chip, 2009. **9**(5): p. 669-676.

37. Squires, T.M. and M.Z. Bazant, *Induced-charge electro-osmosis.* Journal of Fluid Mechanics, 2004. **509**: p. 217-252.

38. Southern, E.M., *Detection of Specific Sequences among DNA Fragments Separated by Gel-Electrophoresis.* Journal of Molecular Biology, 1975. **98**(3): p. 503-&.

39. Gascoyne, P.R.C. and J. Vykoukal, *Particle separation by dielectrophoresis.* Electrophoresis, 2002. **23**(13): p. 1973-1983.

40. Levine, S. and G.H. Neale, *Prediction of Electrokinetic Phenomena within Multiparticle Systems .1. Electrophoresis and Electroosmosis.* Journal of Colloid and Interface Science, 1974. **47**(2): p. 520-529.

41. Grahame, D.C., *The Electrical Double Layer and the Theory of Electrocapillarity.* Chemical Reviews, 1947. **41**(3): p. 441-501.

42. Lehrach, H., D. Diamond, J.M. Wozney, and H. Boedtker, *Rna Molecular-Weight Determinations by Gel-Electrophoresis under Denaturing Conditions, a Critical Re-Examination.* Biochemistry, 1977. **16**(21): p. 4743-4751.

43. Harrison, D.J., A. Manz, Z.H. Fan, H. Ludi, and H.M. Widmer, *Capillary Electrophoresis and Sample Injection Systems Integrated on a Planar Glass Chip.* Analytical Chemistry, 1992. **64**(17): p. 1926-1932.

44. Jackson, J.D., *Classic Electrodynamics*. 3 ed. 1999: John Wiley & Sons. 30.

45. Rossmeisl, J., A. Logadottir, and J.K. Nørskov, *Electrolysis of water on (oxidized) metal surfaces.* Chemical Physics, 2005. **319**(1-3): p. 178-184.

CHAPTER 2

TRAPPING AND STORAGE OF PARTICLES IN ELECTROACTIVE MICROWELLS*

2.1 Abstract

The authors describe electroactive microwells which exploit highly localized electrokinetic effects in order to actively concentrate, confine, store, and reject particles in well defined geometries. In this letter the authors present experimental results demonstrating repeatable trapping and repulsion of polystyrene particles in wells ranging in diameter from 6 to 20 μm in the presence of a superimposed pressure driven flow. A comprehensive finite element model is developed to describe the transport physics involved in the attraction and repulsion processes. Immediate applications include active cell trapping, particle concentration and unlabeled sensing.

* Reprinted with permission from Cordovez, B., Psaltis, D., Erickson D., "Trapping and Storage of Particles in Electroactive Wells", *Applied Physics Letters*, **90**, 024102, 2007.

2.2 Introduction and Device Layout

The ability to deliver individual or small numbers of particles into confined geometries is of great importance for a number of biological applications (including high throughput pathogen detection [1], enhanced sensitivity for surface phase binding assays, [2] parallel single cell trapping, interrogation, and storage [3] and nonbiological applications (including storage of information, directed [4] or passive [5] self-assembly processes, and organic electronics [6]. Within this broader set of devices, microwell arrays have become a popular tool for trapping and storing particles as they enable discrete immobilization of cells without the need for surface binding chemistry (as the trapping site geometry is designed to prohibit trapped particles from dislodging easily) in a simple platform compatible with fluorescence microscopy. Such devices enable not only discrete monitoring of small numbers of specimens [7] but also multiplexed, multiphenotype chemical interrogation without significant cross contamination between closely packed picoliter scale reaction sites [8]. At present, however, these devices rely largely on passive attraction schemes whereby particles are transported solely by sedimentation, capillary, or hydrodynamic forces, all of which represent inherently slow, indiscriminate, and not easily reversible processes.

Integrated microfluidic devices [9] enable accurate particle and bioentity transportation by exploiting their electrical, chemical, and optical properties. The mechanisms that have been implemented in these devices include dielectrophoretic (DEP) (see Rosenthal and Voldman [10], magnetic, entropic, optic, and isoelectric trapping. In this letter we present an active trapping architecture compatible with microwell array formats which enables accurate electrokinetic transport, concentration, and rejection of micrometer sized particles in confined geometries.

Here we present our initial experiments which demonstrate trapping of 1.9 μm diameter polystyrene (PS) beads focusing on developing a description of the fundamental transport physics involved in the trapping and repulsion of the particles. Our approach benefits from the highly localized electric fields that can be generated in electroactive microwells. Since this technique relies on DC electric forces applied on a charged particle, it also enables active repulsion of the trapped targets by reversal of the polarity of the applied field. Although the finite element model presented here is specific to the microwell geometry of interest, the coupling of the electro-osmotic (EO), electrophoretic (EP), and dielectrophoretic transport physics is general to all electrokinetic trapping techniques.

Figure 2.1a shows a schematic of our "electroactive microwells" outlining the basic architecture. The electric field is applied between the upper and lower indium tin oxide (ITO) electrodes, and the wells are defined photolithographically in a polyimide (PI) dielectric. Figure 2.1b is a finite element simulation of the electric field in the well. When a 5 V dc bias is applied, the field becomes concentrated at strengths between 10^5 and 10^6 V/m for a 5 μm deep well, generating extremely large trapping forces in the well. In a quiescent medium, the trapping stability for such a system can be estimated by comparing the work required to dislodge a particle from the well with k_bT via

$$S = qEh/k_bT \tag{2.1}$$

where S is a non-dimensional stability parameter, q is the charge on the particle, and h is the well height channel height). For the polystyrene particles used here we can compute $S = 9\times10^4$, indicating an extremely strong trap (q was obtained from the electrophoretic mobility measurements from Barker *et al*. [11]. Interestingly, q scales

linearly with particle radius, and even for 10 nm diameter particles S is on the order of 500.

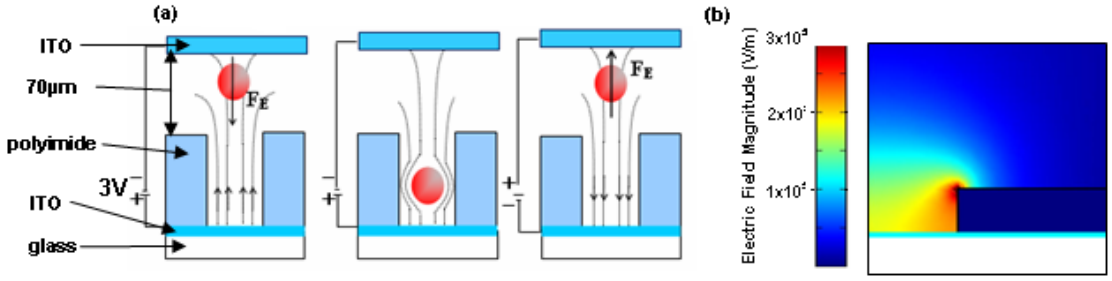

Figure 2.1. Electroactive microwells: (a) Particles are driven, sensed, and repelled from the well depending on the polarity. Microwells with sizes ranging from 6 to 25 μm were patterned on a 5 μm thick spin-on photoactive polyimide dielectric on top of a 8 Ω/sq surface resistivity indium tin oxide coated glass slide. An additional ITO electrode was inserted on top of the wells, separated from the polyimide by two 70 μm spacers, serving to enclose the channel structure and to close the electric circuit. (b) Axisymmetric finite element simulation displaying strong electric field concentration inside the microwell. Color scheme shows increasing electric field strength from blue (lowest) to red (highest).

Figure 2.2 shows our initial trapping experiments using a 0.1 mM phosphate buffer solution at pH 7 containing 1.9 μm diameter polystyrene particles. These particles were carboxyl modified, giving them a negative ζ potential. It is expected that by applying a positive voltage on the bottom electrode the PS beads will be driven from the bulk flow into the well, and they will be ejected by reversing the polarity. Figure 2.2 displays time lapse images of particle trapping and rejection in a 20 μm well for the case of a 5 V applied dc bias and an imposed pressure driven flow of 30 μm/s (average velocity). During the attraction phase, Figures. 2.2a,2.2b,2.2c,2.2d, particles were drawn from the bulk solution into the well over 30 s. Here particles which were either initially positioned or convected into a region approximately three times the diameter of the well would be captured (we refer to this region as the "attraction

basin"). However, particles which approached the well in a plane near the surface were observed to be repulsed from it in an upward and radial direction, implying that additional electrokinetic effects aside from the expected electrophoresis have significant impact on the overall attraction process. Figure 2.2c displays how particles tend to collect at the edges of the wells. As a result of this sidewall collection process, specific well occupancy (as a function of volume) was observed to be much higher for smaller wells under experimental conditions. Smaller wells get filled more since field concentration increases with decreasing well diameter, thus generating a stronger trapping force. When the polarity is reversed, Figures 2.2e,2.2f, particles are repelled out of plane as they approach the well's edge. Particles ejected from the wells form ringlike patterns, suggesting a strong repulsion force that points radially outward from the well's center. The size of the ring shown in Figure 2.2f roughly coincides with the attraction basin, suggesting that particles decelerate due to both the drop in field intensity away from the well and the contribution of viscous drag. While the time scale to fill the well was dependent on the time required for particle convection into the "attraction basin," the rejection time scale was on the order of milliseconds.

A detailed study to characterize the effect of the applied field strength on trapping performance was performed. At the lowest voltage (1.5 V), particles directly in the vicinity of the wells were drawn in, but generally the electrokinetic trapping force was overcome by the hydrodynamic velocity. As we increased the applied potential to 2 V, weak attraction was obtained. At 2.5 V strong particle trapping was first observed. As the applied potential was further increased, the electrophoretic velocity began to strongly dominate over the applied pressure driven flow and the diameter of the attraction basin increased. At applied potentials greater than 5 V the exposed ITO became charred, and electrolysis within the well structure could be observed, representing the highest potential at which the device could be operated. As discussed

by Zhu *et al*. [12] particle adhesion is of significant concern at small scales. We found that plasma cleaning the ITO wells limited the adhesion of polystyrene onto the wells at low voltages. For voltages above 3 V, some particles remained adhered to the ITO even after polarity reversal [as seen in Fig. 2.2e].

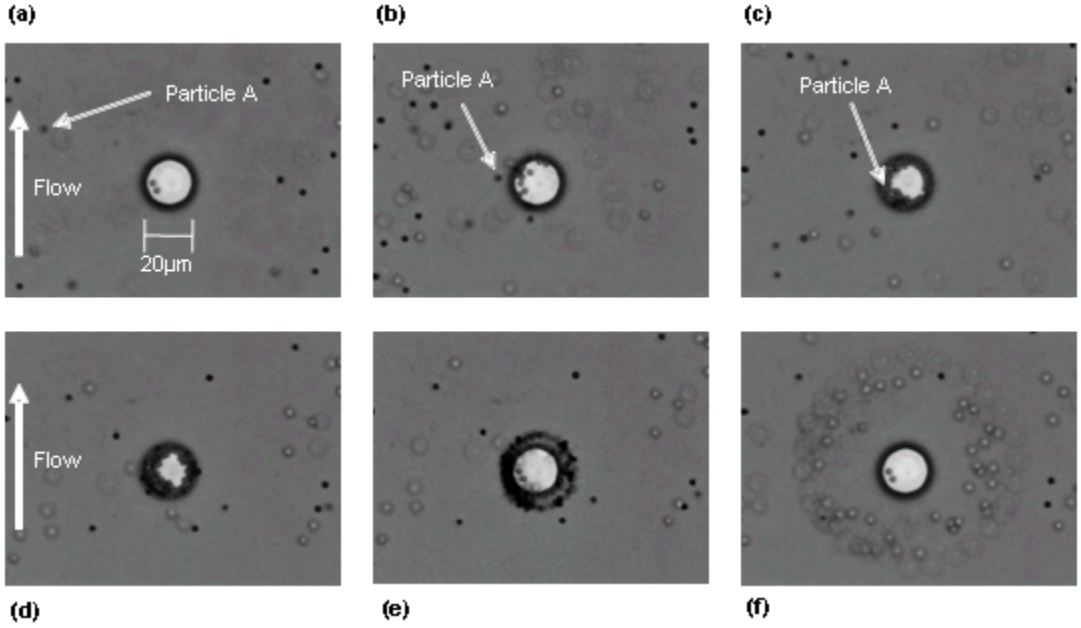

Figure 2.2. Time lapse illustrating particle attraction and repulsion of 1.9 μm polystyrene beads in a 20 μm well. Conditions are a velocity field of 30 μm/s under a 5 V potential. (a) Inactive microwell. Note that two particles adhered onto ITO surface before the experiment was performed. (b) Particle attraction begins and beads are drawn into well. (c) Well after 15 s of attraction. (d) Microwell after 30 s of attraction. (e) Particles are rejected abruptly as polarity is switched. (f) Ring-like pattern remains and drifts due to superimposed velocity field.

2.3 Flow Field Characterization via Finite Element Method

To characterize the coupling and relative strength of the various electrokinetic and convective transport mechanisms, a three-dimensional finite element model of the system was constructed using the microfluidic numerical prototyping techniques

described in our previous works [13]. Briefly the model consists of a simultaneous solution to the constant conductivity electrostatic field:

$$\nabla^2 \phi = 0 \tag{2.2}$$

where ϕ is the applied potential, Stokes flow :

$$\nabla P - \eta \nabla^2 v = 0 \tag{2.3}$$

where p, η, and v are the pressure, kinematic viscosity, and flow velocity, respectively, and continuity

$$\nabla \cdot v = 0 \tag{2.4}$$

equations in a domain with identical geometry to that shown in Figure. 2.2. The solution domain was chosen to be sufficiently large so as to comprise the entire attraction basin. The former of these equations was solved subject to a 3 V potential difference between the top and bottom electrodes (representing the highest trapping force without particle adhesion) and insulating surfaces:

$$\nabla \phi \cdot n = 0 \tag{2.5}$$

where n is the surface normal) at all other boundaries. The Stokes flow and continuity equations were solved subject to a parabolic velocity profile at the inlet and "apparent slip" condition at the polyimide walls by accounting for their electro-osmotic flow. The slip velocity was computed using the Helmholtz-Smoluchowski relation,

$$v_{EO} = -\varepsilon \zeta E / \eta \tag{2.6}$$

where ε is the permittivity of the medium, ζ is the zeta potential of the polyimide/solution interface, taken as −40 mV from Bouriat *et al.*, [14] and

$$E = -\nabla\phi \tag{2.7}$$

is the field strength). Free slip conditions were applied at the side boundaries and normal flow

$$v \cdot n = 0 \tag{2.8}$$

was imposed at the downstream outflow. From this solution the net transport streamlines were computed from the summation of the pressure driven/electro-osmotic flow velocity (vflow), electrophoretic velocity

$$v_{EP} = \mu_{EP} E \tag{2.9}$$

where μ_{EP} is the electrophoretic mobility of the particles, which was computed to be near $4\times10^{-8}\,\mathrm{m^2/V\,s}$ using the zeta potential presented from Barker *et al.*, [11] and dielectrophoretic velocity

$$v_{DEP} = \mu_{DEP} \nabla E^2 \tag{2.10}$$

where μ_{DEP} is the DEP mobility. Figures 2.3a and 2.3b show the net particle transport lines for this case. Near the edges of the well the lines point radially outwards, resulting mainly from the electro-osmotic transport generated at the polyimide surface. Furthermore, the transport lines form a distinct capture region of roughly three well diameters wide, consistent with the attraction basin observed experimentally. The transport lines are skewed to the edge farthest downstream from the well due to the contribution of the pressure driven flow. Further simulations conducted at higher electro-osmotic mobility showed clear recirculation near the well's edge (the extreme case of this is shown in Figure 2.3d) which resulted in a repulsive force on the particles at this location (the local electro-osmotic component acts in the opposite

direction of the electrophoretic attraction). This repulsion is consistent with the experimental observations mentioned above for particles resting on the surface near the well, though the effect tended to be much stronger than what was predicted by our simulations.

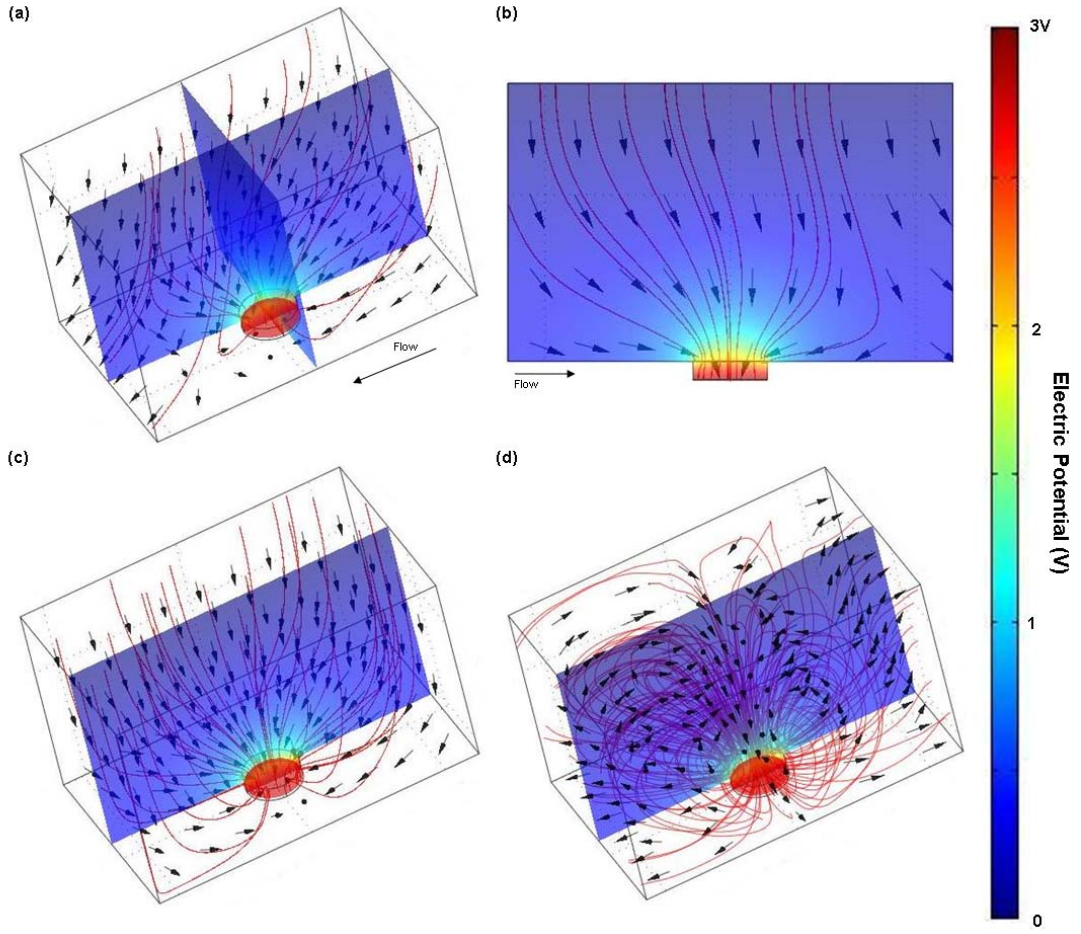

Figure 2.3. Finite element analysis of electrokinetic effects in 20 μm well: (a) Transport lines illustrate competing effects between electro-osmosis, electrophoresis, and dielectrophoresis. (b) Transport lines viewed from cross section. (c) Particle trajectories for charged particles with an uncharged surface. (d) 3D model displaying recirculation induced by dielectric charging.

We believe that the EO transport component may have been enhanced in our experimental system due to dielectric charging at the interface, since increasing ion accumulation in the double layer increases the zeta potential at the polyimide/solution interface. In our model, DEP was found to be small throughout the system except very near the well edges where the field gradients are greatest.

To generalize these observations, we examine how the transport conditions vary as a function of relative contribution of electrokinetic components. The two limiting transport scenarios are presented on Figures 2,3c, 2.3d respectively. Figure 2.3c displays the case of a charged particle in the presence of an uncharged surface (pure electrophoresis). Figure 2.3d illustrates the recirculatory streamlines that arise in the presence of a charged surface guiding uncharged particles (pure electro-osmosis). In general it was observed that at $\mu_{EP,PS}/\mu_{EO,PI} \sim 1.5$, there is still noticeable streamline recirculation, while at $\mu_{EP,PS}/\mu_{EO,PI} \sim 3$ the recirculatory element becomes virtually negligible. Since the EO contribution was generally found to be a hindrance to trapping, a surface treatment could be applied to minimize this component. Although in our current experiment DEP was found to be very small, we expect it to become more significant for well sizes with spatial order below submicrometer dimensions.

2.4 Conclusions

In summary, we have demonstrated electroactive microwells which serve to capture, store, and actively repel particles from confined geometries using a combination of electro-osmotic, electrophoretic, and dielectrophoretic effects. The concentration of the electric field within the well enables high trapping potentials which are suitable for confining particles much smaller than those demonstrated here. The highly concentrated electric field within the well also has the potential to enable

sensitive impedance based sensing, which could be further enhanced by shrinking the size of the confining geometry down to the same spatial order as that of the target.

2.5 Acknowledgments

This work is supported by National Science Foundation through the Sensors and Sensor Networks program under Grant No. NSF/CTS 0529045 and the DARPA Center for Optofluidic Integration at Caltech.

REFERENCES

1. Simmons, B.A., G.J. McGraw, R.V. Davalos, G.J. Fiechtner, Y. Fintschenko, and E.B. Cummings, *The development of polymeric devices as dielectrophoretic separators and concentrators.* Mrs Bulletin, 2006. **31**(2): p. 120-124.
2. Park, M.C., J.Y. Hur, K.W. Kwon, S.H. Park, and K.Y. Suh, *Pumpless, selective docking of yeast cells inside a microfluidic channel induced by receding meniscus.* Lab on a Chip, 2006. **6**(8): p. 988-994.
3. Kang, M.C., L. Trofin, M.O. Mota, and C.R. Martin, *Protein capture in silica nanotube membrane 3-D microwell arrays.* Analytical Chemistry, 2005. **77**(19): p. 6243-6249.
4. Kumar, A., H.A. Biebuyck, and G.M. Whitesides, *Patterning Self-Assembled Monolayers - Applications in Materials Science.* Langmuir, 1994. **10**(5): p. 1498-1511.
5. Cui, Y., M.T. Bjork, J.A. Liddle, C. Sonnichsen, B. Boussert, and A.P. Alivisatos, *Integration of colloidal nanocrystals into lithographically patterned devices.* Nano Letters, 2004. **4**(6): p. 1093-1098.
6. Forrest, S.R., *The path to ubiquitous and low-cost organic electronic appliances on plastic.* Nature, 2004. **428**(6986): p. 911-918.
7. Rettig, J.R. and A. Folch, *Large-scale single-cell trapping and imaging using microwell arrays.* Analytical Chemistry, 2005. **77**(17): p. 5628-5634.
8. Khademhosseini, A., J. Yeh, G. Eng, J. Karp, H. Kaji, J. Borenstein, O.C. Farokhzad, and R. Langer, *Cell docking inside microwells within reversibly*

sealed microfluidic channels for fabricating multiphenotype cell arrays. Lab on a Chip, 2005. **5**(12): p. 1380-1386.

9. Thorsen, T., S.J. Maerkl, and S.R. Quake, *Microfluidic large-scale integration.* Science, 2002. **298**(5593): p. 580-584.
10. Rosenthal, A. and J. Voldman, *Dielectrophoretic traps for single-particle patterning.* Biophysical Journal, 2005. **88**(3): p. 2193-2205.
11. Barker, S.L.R., M.J. Tarlov, H. Canavan, J.J. Hickman, and L.E. Locascio, *Plastic microfluidic devices modified with polyelectrolyte multilayers.* Analytical Chemistry, 2000. **72**(20): p. 4899-4903.
12. Zhu, T., Z.G. Suo, A. Winkleman, and G.M. Whitesides, *Mechanics of a process to assemble microspheres on a patterned electrode.* Applied Physics Letters, 2006. **88**(14).
13. Erickson, D., *Towards numerical prototyping of labs-on-chip: modeling for integrated microfluidic devices.* Microfluidics and Nanofluidics, 2005. **1**(4): p. 301-318.
14. Bouriat, P., P. Saulnier, P. Brochette, A. Graciaa, and J. Lachaise, *A convenient apparatus to determine the zeta potential of grains by electro-osmosis.* Journal of Colloid and Interface Science, 1999. **209**(2): p. 445-448.

CHAPTER 3

ELECTROACTIVE MICRO AND NANOWELLS FOR OPTOFLUIDIC STORAGE[*]

3.1 Abstract

This paper reports an optofluidic architecture which enables reversible trapping, detection and long term storage of spectrally multiplexed semiconductor quantum dot cocktails in electrokinetically active wells ranging in size from 200nm to 5μm. Here we describe the microfluidic delivery of these cocktails, fabrication method and principle of operation for the wells, and characterize the readout capabilities, storage and erasure speeds, internal spatial signal uniformity and potential storage density of the devices. We report storage and erase speeds of less than 153ms and 30ms respectively and the ability to provide 6-bit storage in a single 200nm well through spectral and intensity multiplexing. Furthermore, we present a novel method for enabling passive long term storage of the quantum dots in the wells by transporting them through an agarose gel matrix. We envision that this technique could find eventual application in fluidic memory or display devices.

[*] Reprinted with permission from Cordovez, B., Psaltis, D., Erickson D., "Electroactive Micro and Nanowells for Optofluidic Storage", *Optics Express*, **17** (23), 21134, 2009 . © Optical Society of America.

3.2 Introduction

Recent advances in micro- and nano-fluidics has rekindled an interest in fluid based optoelectronic [1] devices. Within this larger field, several fluidic data storage and logic devices have been recently demonstrated, including that by Thorsen *et al*. [2] where a microfluidic device was used to create an array of discrete chambers which could be probed for the presence of a dye, that by Groisman *et al*. [3] which exploited viscoelastic polymer solutions to create fluidic flip-flops, and that by Prakash *et al*. [4] in which microfluidic bubbles where used to generate an array of universal Boolean logic components. Although these devices have some practical benefits over traditional devices (for example ruggedness to electromagnetic radiation), the fundamental advantage is that they allow the integration of chemical and biological reactions into the logic operation. The main drawbacks of these devices is that the density with which the operations can be stored (on the order of 50 Bs/cm2) is extremely low compared with the state of the art data storage devices [5-8] and the speed with which they operate is currently much slower than state-of-the-art electronics or photonics. While downscaling the fluidic features is the most obvious path to addressing the first of these concerns, the extreme transport speed limitations [9] of nanofluidic devices makes further reduces the speed with which such devices can operate. For example Erickson *et al*. demonstrated the ability to tune the optical output of photonic crystals using nanochannels on the order of 300nm, however they reported very slow switching times limited by the fact that average flow velocity in a nanochannel scales with the square of the channel diameter [10].

Another area of growing research interest is that of visual display technologies. Nanocrystal based displays [11, 12] are being explored due to the unique optical properties of Quantum Dots (QDots) which include ultra sharp colors (narrow

emission line-width) and high quantum efficiency (brightness). Electrofluidic techniques which manipulate custom water dispersed pigments [13] have also been recently used to generate reflective pixels. In another example, Siegel *et al*. [14] demonstrated a disposable, one time use paper based thermochromic display. Consequently, it can be of great interest to establish a technique that is able to exploit the reconfigurability of fluidic based display systems while harnessing the exceptional optical properties of QDots.

Though techniques like dielectrophoresis (DEP) [15] have been used to orient nanoscaled objects and elaborate hybrid electrokinetic techniques [16] have been employed to fluidically direct QDots, the speeds, volume precision and storage density are still below that required to compete with other technologies described above. As a potential approach to addressing this problem, we present here an optofluidic [17, 18] approach for trapping QDots in discrete micro- and nanoscale locations using electrokinetically active wells. In this work we demonstrate the principal of operation for the wells on both the micro- (5μm) and nanoscale (200nm), and experimentally characterize for the first time: the potential storage density through spectral and intensity multiplexing, the storage and erasure speeds, and the internal spatial signal uniformity. We also present a novel method for enabling passive long term non-volatile storage of the quantum dots packets by storing them in wells containing an agarose gel matrix. In the first section below we describe the principal of operation of the device and then apply it to 200nm wells and 5μm wells in sections 3 and 4 respectively. In section 5 we characterize the write and erase times of the device. Finally section 6 describes the non-volatile storage technique.

3.3 Principle of Operation

Figure 3.1 shows an overview of our optofluidic storage device, also available in video format in the Supplemental Information as "optofluidic_data_storage.mov." In the experiments performed here, the QDot storage "packets" are created by mixing solutions of different concentrations of different sized QDots with different fluorescent emission spectra. Since the solution phase concentrations of these QDots maps directly to emission intensity, each unique combination of species at varying concentrations can be related to a unique spectral signal. Once created, the QDot data packet is delivered to an electroactive well site into which it is stored, by applying an electrical potential between the top and bottom electrodes as is displayed in Figure 3.1b. This approach avoids the transport speed limitations of nanofluidic devices by performing the long distance transport in microscale channels and the final storage step only at the nanoscale. To read out the contents of a well, the well is excited using a UV-blue light source and the fluorescent signal collected on a fiber spectrometer. Well depletion can be achieved by reversing the polarity of the field and ejecting the QDots from the wells and into the bulk fluid, then carried downstream by pressure driven flow. Details on the fabrication procedure are provided in Section 3.9.

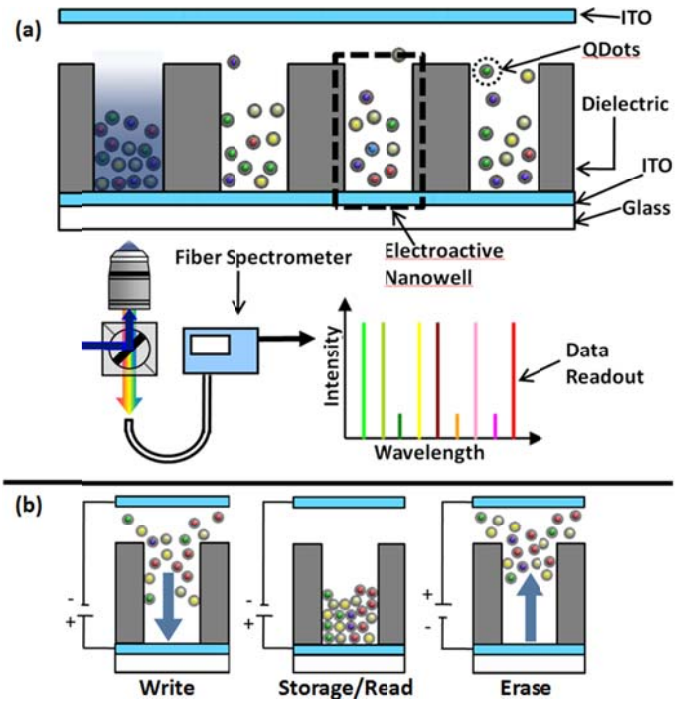

Figure 3.1. Optofluidic Storage of Quantum Dots in Electrokinetically Active Micro- and Nanowells. (a) Quantum Dot (Q Dot) cocktails are delivered by pressure driven flow to an array of electrokinetically active 200nm diameter nanowells. During writing an electrokinetic attraction voltage is applied between the upper surface and the bottom of the nanowell which attracts the QDots into a well as shown in (b). During reading the QDots are optically excited and their emission signal is captured through a fiber spectrometer. (b) Erasing is done simply by reversing the polarity and rejecting the code from the well.

3.4 Quantum Dot Trapping, Storage and Detection in Nanowell Gemotries

In this section we demonstrate the operation of the electroactive nanowell storage elements, as can be observed in Figure 3.2. The wells used in this here are 200nm in diameter and thus consistent with the size of diffraction limited data pits used in traditional planar optical storage media. Figure 3.2a shows the nanowell during electrokinetic attraction, showing a strong emission signal due to QDot accumulation in the base of the well. When the polarity is reversed (as shown in Figure 3.2b) the

QDots are repulsed from the well and the emission intensity decreases. Figure 3.2c shows an optical image of a small portion of the electroactive nanowell array and Figure 3.2d displays an SEM of the nanowell geometry. Because we primarily focus on demonstrating the fundamental storage element, we spaced the wells relatively far apart but note that current lithographic techniques allow for denser bit packing. The repulsion state, Figure 3.2b, shows small background fluorescence, possibly due to particle adhesion, however this can be ameliorated by employing a lower attraction potential and better surface treatments.

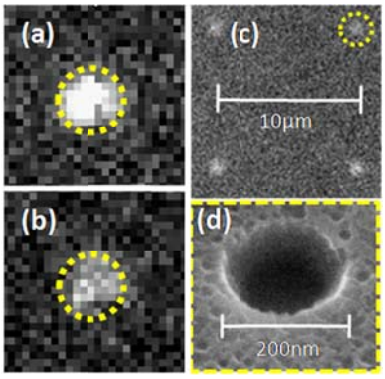

Figure 3.2. Electroactive Nanowells during (a) Electrokinetic Attraction of 4nM solution of 655nm Qdots by applying a 0.8V potential. (b) Repulsion Mode (c) Optical close up of a 2x2 section of the electroactive nanowell array. The top right well is the one shown in (a) and (b). (d) SEM of the 200nm diameter electroactive well, 1µm in depth

The attraction and repulsion sequences displayed in Figure 3.2 can be viewed real time in video "small_well.mov" included in the online supplementary material. Since the colloidal QDots are tagged with Streptavidin (pI ~ 5) they support a net negative electrophoretic mobility in this solution. For the experiments shown above we used a 4nM solution of QDots with a central emission wavelength of 655nm immersed in a

10mM phosphate buffer solution at stabilizing pH of 8.3, under an applied electric potential of ± 0.8V and a mean channel flow velocity of 10μm/s.

Figure 3.3a shows a set of four spectrographic codes obtained from the nanowells. We demonstrate the potential for storing spectrally multiplexed QDot based memory codes by varying the concentration of the 525nm emitting species while keeping the 605nm and 705nm species unchanged. As shown, the peak intensity level of a given species varies approximately linearly with concentration. The intensity of the signals obtained is quite large mainly owing to the high aspect ratio (roughly 5:1) of the nanowells, allowing significant accumulation of QDots in the traps. The large fluorescent signal evidences the strong trapping potentials in these devices [19].

Quantifying the above, in Figure 3b we observe that the intensity counts increase sharply when the attraction potential is applied and similarly decrease sharply when polarity is switched, coinciding with attraction and repulsion of the QDots from the storage sites. We will return to this plot in Section 3.6 to analyze the temporal performance of the devices. Importantly, it can be noted in Figure 3.3b that that the signal degrades from one electrokinetic attraction cycle to the next. This undesirable signal decay is likely due to two effects: The first is that under an applied stimulus (electric potential in our case), charge carriers can be trapped in the QDot matrix, forcing the system out of a light emitting state. Particularly, Gooding *et al*. [20] demonstrated that under a 1 V positive potential (very close to the electric condition inside our wells) and in an acetonitrile electrolyte, the photoluminescence of Cd/Se nanofilms with ZnS shells (similar composition to our QDots) irreversibly quenches with no recovery upon reversal of the electric potential. However, they did not observe this adverse effect for negative potentials. As such we will use QDots tagged with positively charged biomolecules in aqueous pH, or even raise the pH of our current buffer to see if this effect is reduced in future experiments. Moreover, the presence of

an electrolytic reaction at the ITO electrode in the repulsion phase can occur at moderate potentials, lightly charring (darkening) the electrode's surface after every attraction cycle. This could be minimized by using a lower concentration buffer and smaller attraction voltage (both of which serve to reduce the rate of electrolysis), though the latter of these will slow down the temporal performance of the device. Although this represents a limitation of our current approach to nanoscale storage, as will be expanded on in the next section, we have been able to minimize this effect in larger wells.

Since the QDot storage is done in diffraction limited site and the spectral encoding allows for the storage of a large number of signals per well, this device could find use in high density storage applications. QDots are ideal for data storage due to their small size, their narrow emission line-width, their resistance to photobleaching and the ability to excite all species with a UV-blue light source [21]. We note that since this paper focuses is on the nanofluidic manipulation and trapping of QDots in electroactive nanowells, the QDot solutions employed here were generated manually. An automated spectral code writer [17, 22] for discrete QDot cocktail generation was presented in an earlier publication. To demonstrate the potential use of the device in binary storage applications, consider Equation 3.1 which describes the equivalent number of bits N in a single QDot cocktail information packet is given by:

$$N=\log_2 (I^M - 1) \tag{3.1}$$

where I is the number of intensity levels and M is the number of individual species. In the experiment shown in Figure 3.3(a), we show 3 separate species and 4 different intensity levels yielding N=6 separate bits or a 6 fold increase over current single bit media. Existing commercially available QDots exhibit emission spectral with full width half maximums on the order of 50nm and thus we expect that this approach

could sense up to 8 different species emitting from the visible to the IR. If I=M=8, one could read up to 24 bits in a single diffraction limited data site and hence the potential for over an order of magnitude density increase from current surface optical storage technologies. We note that the optofluidic method demonstrated here avoids the tip-to-sample separation problem inherent in near-field and superlensing techniques (which has to be on the order of 10nm due to the exponential decay of the evanescent wave) that have been used in the past to achieve sub diffraction limited data storage [5, 8]. We note that similar QDot optical encoding has previously been demonstrated for biomolecule sequencing [23] and barcoding [24], however this represents the first application directly to data storage. In this demonstration, low nanomolar concentrations helped to reduce the amount of crosstalk between adjacent bits, and note that with greater control over QDot synthesis the number of detectable species could be further increased.

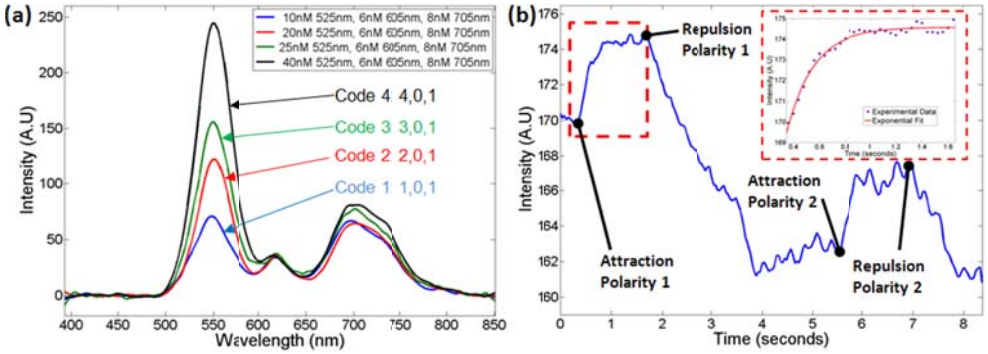

Figure 3.3. (a) Spectrographic readout of simple QDot packets from the electroactive nanowells. Four different codes are shown each consisting of a combination of quantum dot with a central emission wavelength of 525m, 605nm and 705nm. The concentration of the 605nm species was increased in equal amounts from 10nM to 40nM, while the 605nm and 705nm species were held constant. After reading and erasing each bit, it is flushed and the next bit solution is introduced for data readout. (b) Mean fluorescent excitation history in electroactive nanowell during two attraction/storage/repulsion steps. The marks indicate the time in which the polarity of the applied field is switched. Inset shows the fit to the equation $a(1-\exp(-t/\tau))$.

3.5 Extension of Electroactive Well Trapping to Micrometer Scale Geometries

In the next set of experiments we analyze the reversible QDot trapping in 5μm sized electroactive wells in order to demonstrate the applicability of the technique across a range of scales and to examine the spatial uniformity of the quantum dot distribution in the wells. The primary advantage of larger wells is that the ratio of the well base to the volume of the attraction basin is larger and thus the signal to background ratio can be higher. While the spatial density might be too low for memory applications, larger wells could find an application as a fast and spatially uniform technique for pixel writing in nanocrystal displays [11, 12]. Figure 3.4a shows the 5 μm microwell during electrokinetic attraction. Figure 4b shows the decrease in fluorescent intensity after reversing the polarity of the applied field. Figure 3.9 and Figure 3.10 in the supplementary section show the corresponding spectrographic readouts and intensity vs. time trace for this size well. In Figure 3.4c we present the spatial uniformity of the QDot emission from inside the large microwell. As can be seen, the emission intensity remains relatively flat along most of the radius of the well but begins to drop off towards the edge. In our previous work we have shown that electroosmotic transport leads to recirculation inside the walls of the electroactive wells [19], resulting in increased accumulation of particles on the well edges. However, in Figure 3.4c it can be appreciated that since the emission is spatially uniform except near the edges, the dominant transport effect is electrophoresis rather than electroosmosis. This is expected since the moderately high buffer concentration strongly suppresses the Debye layer, thus diminishing electroosmotic effects. For display applications, this will minimize localized QDot clustering at the well edges leading to a more uniform distribution.

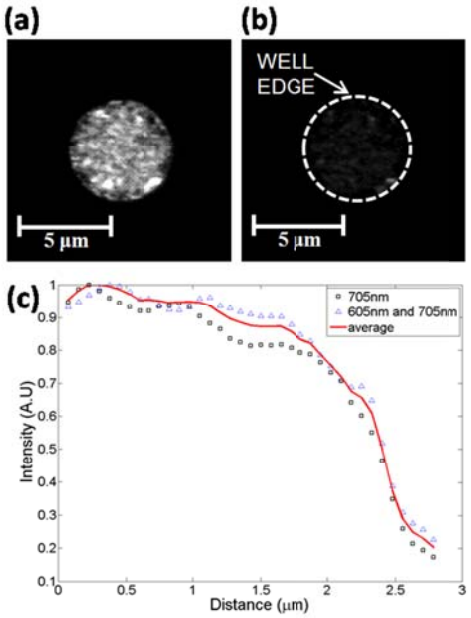

Figure 3.4. Large electroactive microwell during (a-b) Attraction and rejection of a mixture containing 3 nM 705nm with 6nM 605nm emitting QDots (c) Radial distribution of fluorescent intensity inside microwell. The cocktail used here contained 3 nM 705nm with 6nM 605nm emitting QDots at pH=8.3. This solution was delivered to the well at an average flow speed of 40µm/s and then trapped by applying a 0.8V potential.

3.6 Device Temporal Characterization and Well Spatial Density Analysis

In this section we characterize the trapping (or write) and repulsion (or erase) time scales as a function of the flow conditions and well dimensions. To do this, the average intensity from the wells during the attraction phase was fit to an exponential relation $a(1-\exp(-t/\tau))$. A sample fit is shown in the inset of Figure 3.3b) where a is a fitting parameter, t is the elapsed time and τ is the characteristic time constant for well filling saturation. This was used as the parameter to characterize write speed of the device. For an attraction voltage of 0.8V, the smallest time constant achieved for the nanowells was 153ms at a mean flow speed of 43µm/s. Plotting the measured time constants as a function of the transport velocity in Figure 3.5 shows a decreasing trend

in the time constant with increasing flow speed. A linear fit to the data shows that for every increase of 1 μm/s in average channel velocity, the trapping time constant decreases by 7 ms. As such the write speed could be significantly improved by increasing the transport flow velocity. The reason the writing speed increases with velocity is that the mass flux of entering the attraction basin of a given well increases. For the larger wells (see inset in Figure 3.5) the trapping time is longer but the dependence on flow speed is much higher. This is because the attraction basin of the larger wells is bigger and thus is more effective in attracting nanoparticles from farther away. The smallest erase time scale recorded was measured to be less than 30ms, (see Figure 3.10).

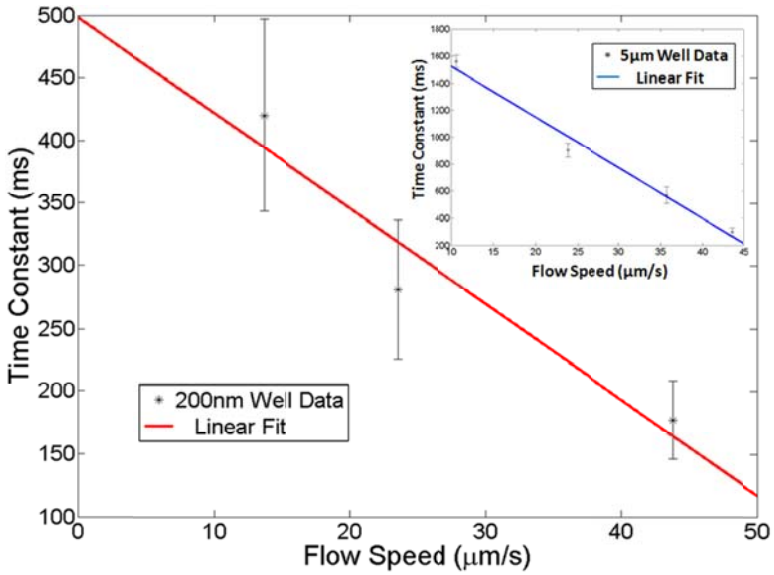

Figure 3.5. Attraction time scales vs. mean channel velocity. The time scale data was obtained by performing exponential fits to the time intensity data. The red linear fit is made for the 200nm electroactive well data while the blue linear fit in the inset displays the trend for the 5 μm well data.

It is important to note that there have been many important advancements using nanoparticles in optical data storage, particularly focusing on exploiting surface

plasmon interactions in metallic nanorods to multiplex in the wavelength, polarization and spatial domains [25, 26]. While these devices potentially offer higher storage densities and very fast data storage and retrieval, our device enables multiplexing while also permitting data to be rewritten and does not require expensive pulsed laser setups. Furthermore, while the reported serial write time for our device of 40 bit/second is much lower than other storage devices, it is important to note that one of the key attributes of our device is that it enables simultaneous data as well as chemical storage. It can therefore serve as an interface between large scale chemical and biological integration and computation. In this respect, it is important to consider the time scales involved in traditional biochemical sensing platforms as well. For example, a reliable DNA chip test can take on the order of days (~10^5 s) due to its diffusion limited transport. Our device is capable of transferring material on the order of 10^{-1} s which lies roughly halfway between the above and that for established pure data storage techniques (~10^{-8} s). The reported write time also allows us to place limits on the theoretical highest achievable bit density that does not exhibit diffusion based cross talk between neighboring storage. Given our current 150ms write time, a first order calculation using Fick's diffusion length, $L_{space} = (4Dt)^{1/2}$, using the diffusion coefficients, D, reported in Chen *et al.* [27] leads to L_{space} = 770nm which is roughly twice the minimum blu-ray pitch (320nm). With our demonstrated factor of 6 improvement, this gives us a 1.5 fold increase in storage density over single layer blu-ray using physical matter. By decreasing the write time to 25ms or increasing the storage density to 24-bit/well a 6 fold improvement would be possible.

3.7 Non-Volatile Storage Using an Agarose Gel Matrix

Both the micro- and nanoscale storage devices described above are volatile in that an external voltage needs to be continuously applied to sustain QDot retention. Without this applied electric potential, QDots will diffuse out of the well and the fluorescence signal is lost in a relatively short time. In order to extend this signal retention, we coated the microwells with a thin agarose hydrogel which will inhibit nanoparticle diffusion. Figure 3.6a shows the nonvolatile device operation schematic. As before, QDot cocktails are fluidically delivered to the vicinity of an agarose coated electrokinetic well. The electric potential is then applied between the top and bottom ITO electrodes, generating a confined electric field inside the microwell. The resulting electrokinetic forces drive the particles inside the wells through the nanoscale pores in the agarose gel. Figure 3.6b displays an SEM illustrating a gel covered well; with a pore size near 200nm for a 1% weight by volume (roughly matching the results of Narayan *et al.* [28]. An SEM of the cross section of the well geometry can be found in Figure 3.11. As will be shown below, just like in the uncoated scenario, the wells can be depleted by reversing the polarity and ejecting the QDots to the bulk fluid. Such a coating was easier to employ in the microwell geometries, which is why this technique was not used in the nanowell case.

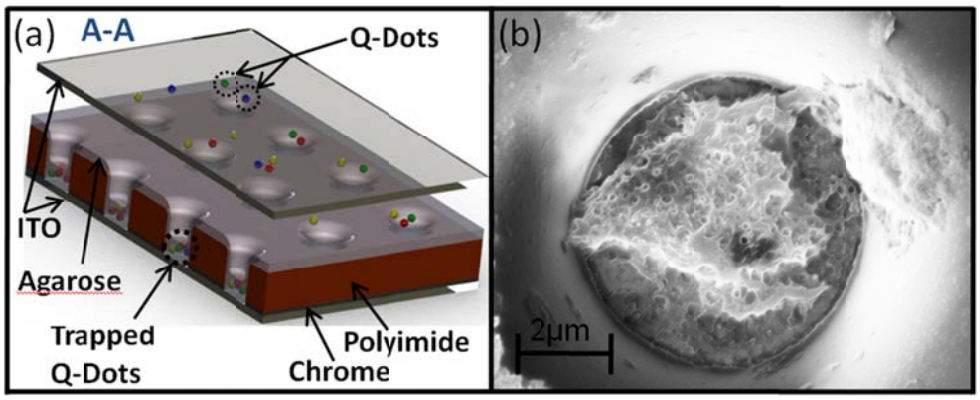

Figure 3.6. (a) Non-volatile storage device schematic (x-section view). QDots are trapped in the wells and through the nanoscale pores of the gel (b) SEM of gel covered microwell for a 1% w/v coating.

Figure 3.7 illustrates how the mean fluorescent intensity varies for attraction and repulsion sequences at various gel concentrations (and therefore pore sizes). Just like in the nanoscale wells, the attraction setting results in the localization of the QDots inside the wells and is observed as an increase in mean fluorescent intensity and the opposite occurs for electrokinetic repulsion. These characteristic time scales of these processes are also presented in Table 3.1.

Table 3.1. Time Scale Summary of Microwell Traps

Agarose [%w/v]	Pore Size[a] [nm]	Attraction [ms]	Repulsion [ms]	Retention [sec]
0	N/A	343 (± 38)	193 (± 35)	178 (± 35)
0.5	~500	434 (± 58)	215 (± 46)	3752 (± 524)
1	~200	405 (± 82)	226 (± 79)	3120 (± 784)
1.5	~100	822(± 157)	391 (± 92)	>5000[b]

[a]From Narayan *et al.* Reference [28]
[b]Photo -Bleaching Limited

The first result here is that for gel concentrations varying from 0 to 1% w/v, though the attraction and repulsion times tend to increase (slower response) with decreasing pore size, the overall change is not great. The similar time scales likely result due to the fact that since even for the smaller pores at 1% (~200nm when fully hydrated) this is still at least ten times greater in size than a QDot diameter. Furthermore, the sizes of the pores are also large enough so that Debye Layer proximity (for this 1mM solution the Debye length is on the order of 10nm) will not result in significant flow retardation. However, during the overnight gel dehydration process (explained in the Experimental Section) at the increased 1.5% w/v setting, the result is likely unstable pore formation, leading to their shrinking and collapsing. Thus, the attraction process is roughly 2.4 times slower for the high sugar concentration scenario when compared to the rest. It will be noted below, however, that the signal retention time under no external voltage will be greatly enhanced for this same gel concentration. As is also shown in Figure 3.7, for gels with agarose concentrations 1%w/v and below, the attraction and repulsion processes are almost entirely reversible. At the 1.5%w/v scenario, it was found that there was heavy non specific adsorption of the QDots onto the gel, which is manifested as a fluorescent accumulation between attraction and repulsion cycles. Though treating this gel type with surfactants may be of interest to reduce this accumulation, our results indicate here the gel is becoming effectively saturated and solidified.

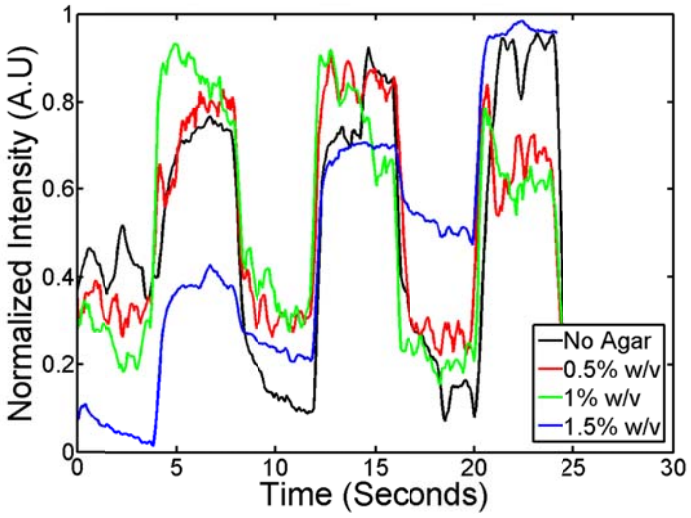

Figure 3.7. Mean fluorescent excitation history in an electroactive microwell with gel coatings at various agarose concentrations during a sequence of attraction and repulsion steps.

Figure 3.8 illustrates the how the QDot retention varies as a function of pore size. In this experiment, the particles are delivered to the well sites, and after 3 minutes, a 1V attraction potential is applied and immediately turned off. For the uncoated scenario, the QDot diffusion out of the well effectively depletes the fluorescent intensity in less than three minutes, making this scenario less useful for long term storage at lower power cost. The retention time scales, here defined as the time it takes the fluorescent signal to decay to half of its fully saturated value, are also shown in Table 1. For the 0.5% and 1% w/v, similar retention times on the order of an hour were observed, representing nearly a twenty-fold increase over the uncoated case. For the 1.5% w/v case, retention times were typically greater than 5000s. As mentioned before, this scenario offers the best retention characteristics, but exhibits a slower electrokinetic response and also suffers from undesirable nonspecific adsorption.

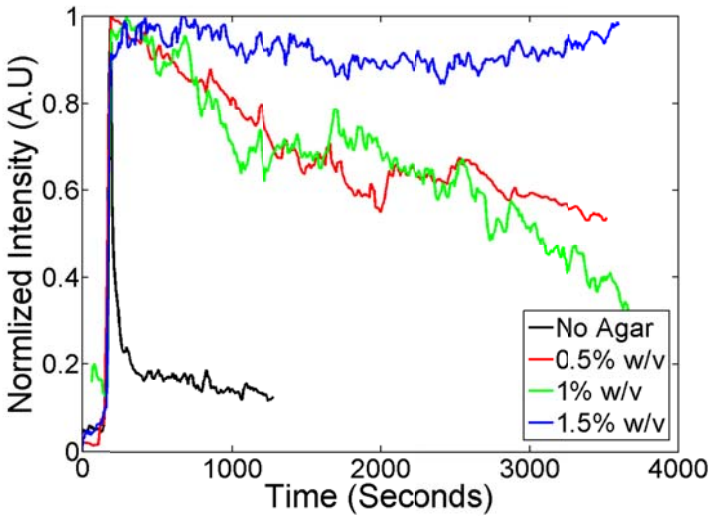

Figure 3.8. Fluorescent signal retention history as in an electroactive microwell with gel coatings at various agarose concentrations. A 1V potential is applied at the 180 second mark and instantaneously switched off.

3.8 Outlook and Conclusions

In summary, we have demonstrated and characterized here a new micro- and nanofluidic approach to physical storage of spectrally and intensity multiplexed Quantum Dot packets. In addition to introducing the devices, we show the potential for exceeding the storage limits of single-layer diffraction limited optical storage media by between 1.5 and 6 fold, and report data read and erase times of 153 and under 30 milliseconds respectively. We also demonstrate and characterize a technique for enabling non-volatile storage of the Q-Dot packets using an agarose gel matrix. With this technique, passive retention times greater than 1hr are demonstrated.

We focused here on demonstrating the important basic storage element and the potential behind the technology, however in order to create a fully integrated device there are several future technical challenges which must be addressed. Among the most important of these are continuous rewritability and individual well addressability.

An integrated device must achieve continuous rewriteability in that after a data cocktail is erased, one must break the data packet of interest into its basic units so that it can be returned to the spectral code writer [17, 22]. We show how this could be accomplished in Figure 3.12 where an initially homogeneous data packet is separated into its constituent red, yellow and green colors using electrophoresis since the smaller sized quantum dots migrate faster downstream than the larger ones. With regards to the second challenge, although electrical addressability on the scale of that required here to address individual arrays of 200nm diameter wells is well within the fabrication limits of current CMOS technology, additional complications are expected such as device alignment and inter-well electrical cross talk. In future versions of the device we hope to address some of these concerns.

3.9 Supplementary Figures

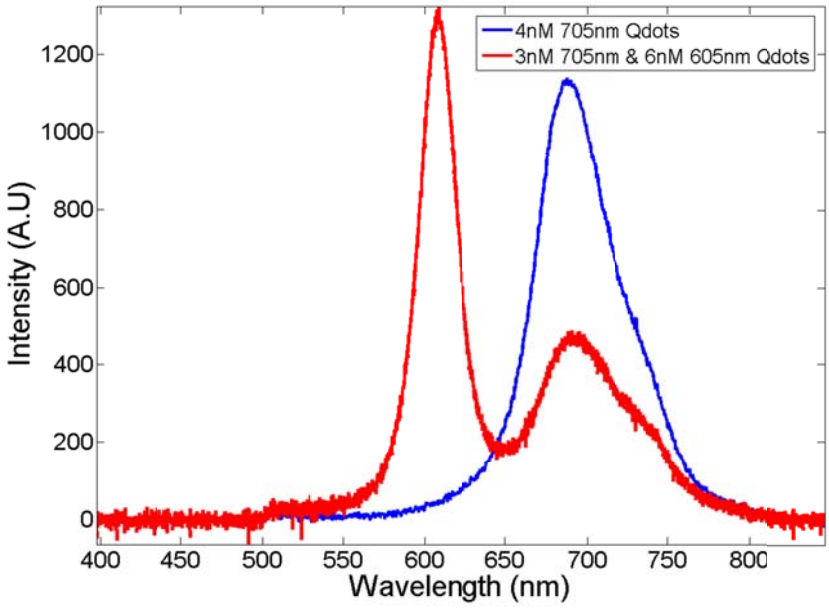

Figure 3.9. Fluorescent signal retention history as in an electroactive microwell with gel

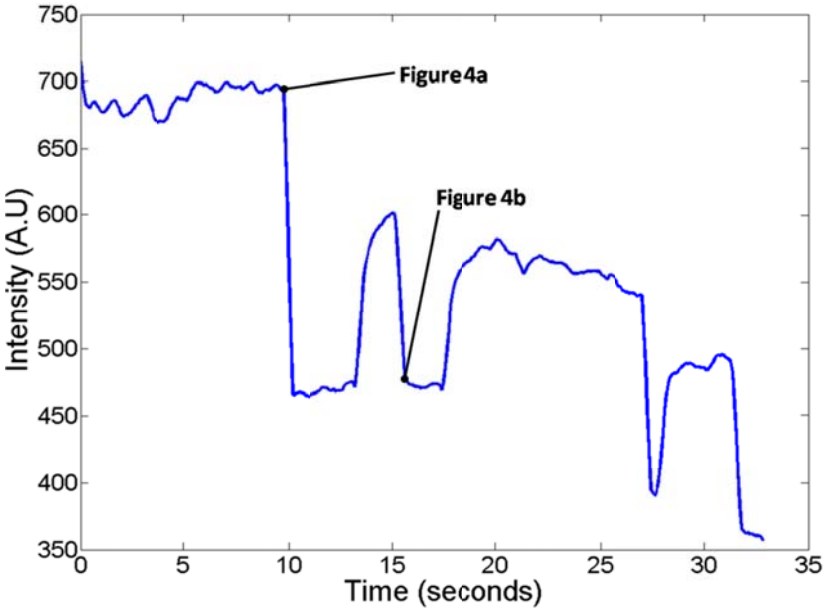

Figure 3.10. Mean fluorescent intensity vs. time trace for electroactive microwell shown in Figure 3.4.

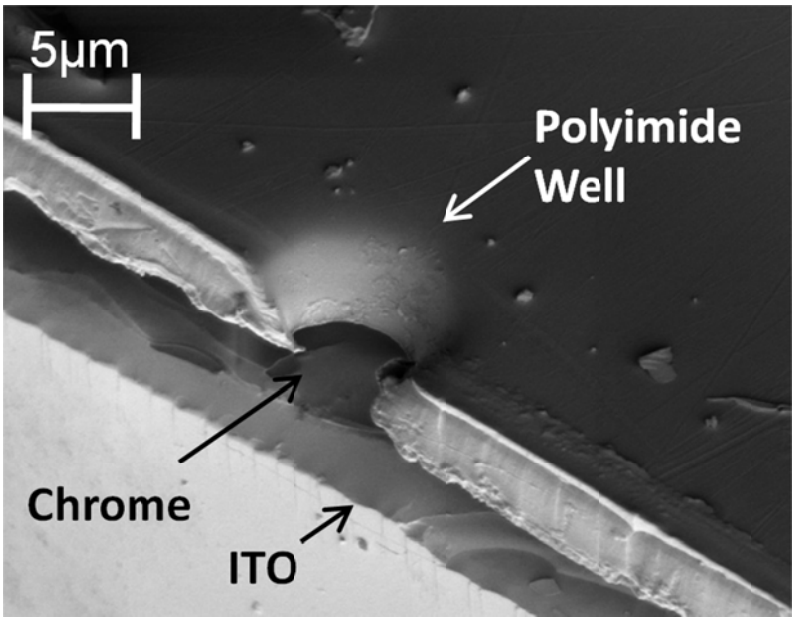

Figure. 3.11. SEM of the cross section of the electroactive microwell geometry previous to chrome layer etching. This alternative method is chosen due to ease of use and reduction of fabrication steps.

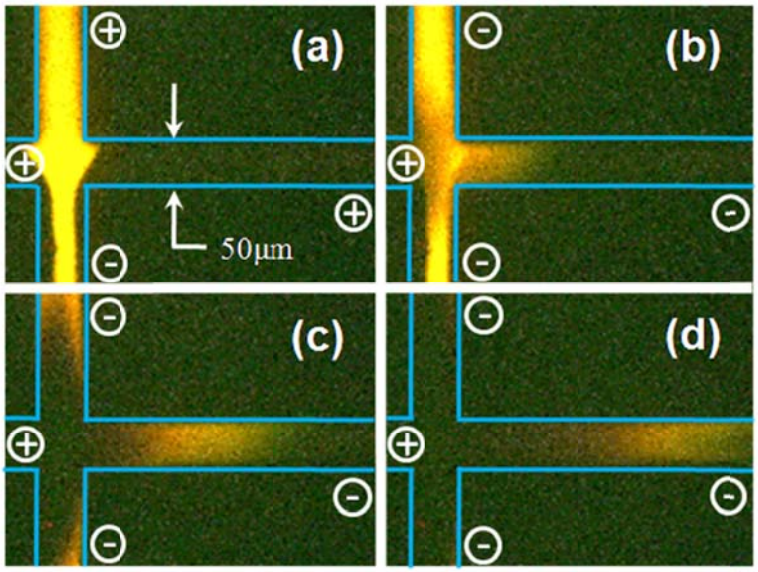

Figure 3.12. Homogeneous data packet is being separated into its constituent red, yellow and green colors using capillary electrophoresis. Smaller sized quantum dots migrate faster downstream than the larger ones, suggesting that after bit erasure one could separate a data packet into its fundamental parts for reuse.

3.10 Materials and Methods

3.10.1: Electroactive Nano and Microwell Fabrication:

A thin 8-12 ohm ITO coated coverslip (SPI Supplies) was coated with a 40nm chrome layer, a 200nm thin oxide stop layer, a 600nm silicon body and a 280nm oxide mask. Wells 200nm in diameter were patterned on the substrate with PMMA (Polymethyl methacrylate)) based resist through electron beam lithography, followed by a sequence of reactive ion etches and a final wet chrome etch, leaving the ITO layer exposed. ITO was chosen as the bottom transparent conductor in order to enable fluorescent excitation from below the substrate [19]. Additional details of the fabrication can be found in the Supporting Information under Electroactive Nanowells Fabrication.pdf.

Though the same technique can be used to pattern the larger sized wells, a simpler fabrication technique as shown in Figure 3.6. Electrically active microwells (5 μm radius by 5 μm tall) where fabricated on top of an ITO coverslip and a 100nm chrome layer by using spin on positive photoactive polyimide (HD MicroSystems 8820). The microwells were patterned and developed, followed by a quick chrome etch, which results in clear, conductive wells surrounded by an opaque layer which blocks polyimide self-fluorescence during irradiation. We note that the silicon/oxide and polyimide based dielectrics did not lead to changes in the QDot transport and both served as good insulators.

3.10.2: Non Specific Adsorption Treatment, QDot Solutions and Agarose Coating Preparation:

After well fabrication, the substrate was cleaned with oxygen plasma, and left overnight at room temperature shaking in a 5ml toluene solution containing 50 µl PEG (Polyethylene Glycol) - Silane, and 50 µl of a Triethylamine catalyzer. The chip was then rinsed in toluene and baked at 80°C for 2 hours to polymerize the PEG silane. Discrete nanocrystal cocktails were created by mixing different nanomolar concentrations of different species of Streptavidin (pI~5) modified CdSe (ZnS shell) QDots (Invitrogen Corp.) in a 1mM solution of DI water solution of pH=8.3. Since we focus here on the data storage challenges, the QDot solutions employed were generated manually and offline. A QDot spectral code writer for active QDot mixing was presented in an earlier paper [17, 22]. It is important to note that fluorescent excitation was not performed with a regular UV-Blue QDot filter, but with a green (525nm) excitation filter instead. This served to help reduce any potential bleaching of the already robust QDots.

Using a high melting temperature gel 70°C (Omnipur), thin agarose gel membranes where prepared by mixing different solution phase concentrations of agarose (0.5%, 1% and 1.5% w/v) with 1mM DI water at pH=8.3 followed by heating to 120°C for 20 minutes. 5 µl of the heated solution was pipetted on top of the wells and left at room temperature overnight, resulting in a thin and nearly uniform membrane measuring from 2.5 to 3µm on top of the wells.

3.11 Acknowledgments

This work is supported by National Science Foundation through the Sensors and Sensor Networks program under Grant No. NSF/CTS 0529045 and by the Defense Advanced Research Projects Agency through the Center for Optofluidic Integration funded under the University Photonics Research program.

REFERENCES

1. Vlassiouk, I. and Z.S. Siwy, *Nanofluidic diode.* Nano Letters, 2007. **7**(3): p. 552-556.
2. Thorsen, T., S.J. Maerkl, and S.R. Quake, *Microfluidic large-scale integration.* Science, 2002. **298**(5593): p. 580-584.
3. Groisman, A., M. Enzelberger, and S.R. Quake, *Microfluidic memory and control devices.* Science, 2003. **300**(5621): p. 955-958.
4. Prakash, M. and N. Gershenfeld, *Microfluidic bubble logic.* Science, 2007. **315**(5813): p. 832-835.
5. Betzig, E., J.K. Trautman, R. Wolfe, E.M. Gyorgy, P.L. Finn, M.H. Kryder, and C.H. Chang, *Near-Field Magnetooptics and High-Density Data-Storage.* Applied Physics Letters, 1992. **61**(2): p. 142-144.
6. Dhar, L., K. Curtis, and T. Facke, *Holographic data storage: Coming of age.* 2008. **2**(7): p. 405.
7. Coufal, H.J., D. Psaltis, and G. Sincerbox, *Holographic Data Storage*. Springer Series in Optical Sciences. Vol. 76. 2000: Springer-Verlag.
8. Zhang, X. and Z.W. Liu, *Superlenses to overcome the diffraction limit.* Nature Materials, 2008. **7**(6): p. 435-441.
9. Burgreen, D. and F.R. Nakache, *Electrokinetic Flow in Ultrafine Capillary Slits.* Journal of Physical Chemistry, 1964. **68**(5): p. 1084-&.
10. Erickson, D., T. Rockwood, T. Emery, A. Scherer, and D. Psaltis, *Nanofluidic tuning of photonic crystal circuits.* Optics Letters, 2006. **31**(1): p. 59-61.

11. Gao, M.Y., J.Q. Sun, E. Dulkeith, N. Gaponik, U. Lemmer, and J. Feldmann, *Lateral patterning of CdTe nanocrystal films by the electric field directed layer-by-layer assembly method.* Langmuir, 2002. **18**(10): p. 4098-4102.

12. Sun, Q., Y.A. Wang, L.S. Li, D.Y. Wang, T. Zhu, J. Xu, C.H. Yang, and Y.F. Li, *Bright, multicoloured light-emitting diodes based on quantum dots.* Nature Photonics, 2007. **1**(12): p. 717-722.

13. Heikenfeld, J., K. Zhou, E. Kreit, B. Raj, S. Yang, B. Sun, A. Milarcik, L. Clapp, and R. Schwartz, *Electrofluidic displays using Young-Laplace transposition of brilliant pigment dispersions.* Nature Photonics, 2009. **3**(5): p. 292-296.

14. Siegel, A.C., S.T. Phillips, B.J. Wiley, and G.M. Whitesides, *Thin, lightweight, foldable thermochromic displays on paper.* Lab on a Chip, 2009. **9**(19): p. 2775-2781.

15. Li, J.Q., Q. Zhang, N. Peng, and Q. Zhu, *Manipulation of carbon nanotubes using AC dielectrophoresis.* Applied Physics Letters, 2005. **86**(15).

16. Sin, M.L.Y., V. Gau, J.C. Liao, D.A. Haake, and P.K. Wong, *Active Manipulation of Quantum Dots using AC Electrokinetics.* Journal of Physical Chemistry C, 2009. **113**(16): p. 6561-6565.

17. Psaltis, D., S.R. Quake, and C.H. Yang, *Developing optofluidic technology through the fusion of microfluidics and optics.* Nature, 2006. **442**(7101): p. 381-386.

18. Monat, C., P. Domachuk, and B.J. Eggleton, *Integrated optofluidics: A new river of light.* Nature Photonics, 2007. **1**(2): p. 106-114.

19. Cordovez, B., D. Psaltis, and D. Erickson, *Trapping and storage of particles in electroactive microwells.* Applied Physics Letters, 2007. **90**(2).

20. Gooding, A.K., D.E. Gomez, and P. Mulvaney, *The effects of electron and hole injection on the photoluminescence of CdSe/CdS/ZnS nanocrystal monolayers.* Acs Nano, 2008. **2**(4): p. 669-676.

21. Bruchez, M., Jr., M. Moronne, P. Gin, S. Weiss, and A.P. Alivisatos, *Semiconductor Nanocrystals as Fluorescent Biological Labels.* Science, 1998. **281**(5385): p. 2013-2016.

22. Erickson, D. *Spectrographic microfluidic memory*. in *Proc. ICMM*. 2005. Canada.

23. Han, M.Y., X.H. Gao, J.Z. Su, and S. Nie, *Quantum-dot-tagged microbeads for multiplexed optical coding of biomolecules.* Nature Biotechnology, 2001. **19**(7): p. 631-635.

24. Chang, S., M. Zhou, and C.P. Grover, *Information coding and retrieving using fluorescent semiconductor nanocrystals for object identification.* Optics Express, 2004. **12**(1): p. 143-148.

25. Mansuripur, M., A.R. Zakharian, A. Lesuffleur, S.H. Oh, R.J. Jones, N.C. Lindquist, H. Im, A. Kobyakov, and J.V. Moloney, *Plasmonic nano-structures for optical data storage.* Optics Express, 2009. **17**(16): p. 14001-14014.

26. Zijlstra, P., J.W.M. Chon, and M. Gu, *Five-dimensional optical recording mediated by surface plasmons in gold nanorods.* Nature, 2009. **459**(7245): p. 410-413.

27. Chen, C., S.L. Liu, R. Cui, B.H. Huang, Z.Q. Tian, P. Jiang, D.W. Pang, and Z.L. Zhang, *Diffusion Behaviors of Water-Soluble CdSe/ZnS Core/Shell Quantum Dots Investigated by Single-Particle Tracking.* Journal of Physical Chemistry C, 2008. **112**(48): p. 18904-18910.

28. Narayan, J., J.Y. Xiong, and X.Y. Liu, *Determination of agarose gel pore size: Absorbance measurements vis a vis other techniques*. Journal of Physicals: Conference Series, 2006. **28**: p. 83-86.

CHAPTER 4

HYBRID CHEMICAL-ELECTRIC CONTROL OVER FLYING BIO-ROBOTIC SYSTEMS[*]

4.1 Abstract

To date, Insect Micro-Air vehicle [1] flight operation has been traditionally manipulated through purely electronic control schemes that influence neuromuscular activity [2-7]. Though these techniques enable tight control of flight maneuverability, there is a drive to integrate additional functionality to perform procedures that include remote sensing, [8] power harvesting [9, 10] and complete physiological control through chemistry [11]. Here we demonstrate for the first time a wireless and hybrid control approach that fuses the previously established electrical control schemes with an implantable microfluidic drug delivery system [11] that can release neurotransmitters on command to alter the locomotive activity of Manduca Sexta moths. We present hybrid flight manipulation procedures including takeoff and sustained flight of the insect through DC electrical stimulations, and chemical controls ranging from deceleration to full paralysis through the microfluidic ejection of 15 µL an L-Glutamic acid solution. We show the reversibility of our process since chemical payloads can be used to override the electrical stimuli, while electrical stimuli enable quicker recovery from chemically induced paralysis.

[*] To be submitted for publication to *Nature* by Cordovez, B[‡]., Chung, A.J[‡]., Huang, X.T., Jasuja, N., D., Erickson D., "Hybrid Chemical-Electronic Control Over Flying Bio-Robotic Systems"

[‡] Contributed equally to this work

4.2 Introduction

Advancements in MEMS technology [12] have allowed the generation of minute flying robotic systems with biomimetic [13] characteristics like Wood ’s flying Diptera robot [14] with a wingspan under 4 cm. The downscaling of micro-air vehicles, however, has presented severe challenges since aerodynamics are compromised in the small scales, resulting in high power requirements to lift the main body and battery weights [1]. Flying insects on the other hand have solved this coupled problem since they evolved to be aerodynamically efficient [15, 16] and feed for weeks during metamorphosis, but attempts to train and control them directly have proved challenging [17]. As such, a new genre of hybrid bio-robotic systems emerged based on the fusion of electronic systems with the neural interfaces of flying insects and has raised much research interest [18] for an array of areas including remote surveillance [8] and power harvesting [9, 10].

To this day, the paradigm for hybrid insect flight manipulation has been microelectronic based control of neuromuscular activity by interfacing electronics with the insect’s nervous system [3]. Aerodynamic operations including liftoff, yaw control, landing [2], and even controlled terrestrial walking patterns [4] have been demonstrated by Bozkurt *et al*. through wireless DC pulses directed to the antennal lobe and wing muscles of a Manduca Sexta moth. Tsang *et al*. [6] enabled flight steering in the same type moth by controlling abdominal orientation using a flexible electrode ring attached to the nerve cord. Even different insects like Cotinis Texana beetles have also been electrically manipulated to perform liftoff, landing and flight elevation maneuvers as shown by Sato et al. [5, 7]. Though these techniques offer great control for flight maneuverability, electronic approaches have power constrain issues in long term stopping procedures since orders need to be constantly streamed to

keep the insect at rest, and moreover, these approaches do not readily exploit the already present chemical machinery which controls both the insect's locomotion as well as its overall physiology.

Fluidic payloads which contain chemical and biological agents provide a complementary set of advantages to the aforementioned electrical stimuli. Ziegler *et al*. [19, 20] showed that adult Manduca Sexta moths that feed on sugar water can live longer, and females can lay more eggs. Experiments also indicate that the locomotive activity of these insects can be enhanced through the delivery of octopamine and pilocarpine [21, 22] neurotransmitters, both of which trigger regular firings of single motor neurons resulting in characteristic flight motor patterns even without sensorial input. Interestingly, while chemical fuels are the norm for traditional land and air vehicle locomotion, there is only one attempt to use chemical agents for micro-air vehicle locomotive control as demonstrated by Chung and Erickson [11]. There we demonstrated the temporary paralysis of a tethered Manduca sexta moth through the delivery of various neurotransmitter solutions through an immaturely implanted microfluidic chip. In this paper, we build on that technique and the previous milestones in electrical control to generate a hybrid architecture that exploits the advantages of both approaches for the control of a Manduca Sexta moth. Here we demonstrate, for the first time, a synergistic utilization of chemical and electrical stimulations, and characterize the moth's response and performance to various electrical and chemical stimuli via a locomotive performance analysis by tracking their displacements through an indoor GPS system.

4.3 Device Layout and Operation

The full scale hybrid system is presented conceptually in Figure 4.1a and the corresponding experimental setup is shown in Figure 4.1b. Briefly a commercial wireless microcontroller with multiple independent electrical output ports is used to trigger both the electrical stimuli and the microfluidic chip actuation. This microfluidic chip (Figures 4. 1c.i through 4.1c.iii) is implanted on the moth's dorsal thorax and works on an electrochemical pumping procedure that was previously demonstrated by Chung *et al*. [23]. Briefly, chlorine ions in the buffer react with a capping gold membrane on top of the fluidic chip, forming a water soluble chloro-gold colloid. In addition, water electrolysis breaks the liquid into gas which builds up the pressure in the enclosed chamber, leading to mechanical failure of the capping membrane and finally pressure is relieved through the ejection of the fluidic contents to the outside environment. Since the microcontroller can only output a 3V battery voltage, the anode of the microfluidic chip was connected to a 34V DC to DC converter, which supplies a larger load and thus increases the reaction rate; while the bottom electrode of the fluidic chip is connected to a universal ground. The new version of this chip is 4 times smaller than its predecessor while still capable of carrying the same volumetric payload. This was achieved by reducing lithographic pattern dimensions as well as implementing a custom 3D printed acrylic channel to hold the chemical payloads. Please refer to the Materials and Methods Section 4.5.1 for more details on Fabrication. Figures 4.1c.i through 4.1c.iii show an 80 second time lapse of the fluidic ejection of a 5M L-GA solution into 10 mM Phosphate buffered Saline (PBS). In this time lapse, the solution bursts out of the capping gold membrane at a speed of nearly 10cm/s and the chip is almost empty at the 80 second mark. For the electrical stimulation, a secondary output port of the wireless microcontroller was

implanted in the moth's antennal lobe (Figure 4.1a and 4.1b) via a thin copper wire, while the corresponding ground is the universal electrode located in the moth's dorsal thorax. Even though further miniaturization of the wireless components has been already demonstrated [2, 5, 6], here we primarily focus on the integration of chemical and electrical control schemes. As such, we used the buoyant force generated by a 6L helium balloon to compensate for the weight of the circuitry (6g), since on average a Manduca Sexta can lift its body weight plus an additional gram of payload [2]. Figure 4.1d shows a CT scan 3D reconstruction of a Manduca Sexta with the implanted chip in its dorsal thorax, where we note that the chip penetrated about 2 mm into the thorax, bringing the chemical payloads close to both the central nervous system and the main circulatory system for effective drug delivery. For details on the chip implantation procedure, please refer Materials and Methods Section 4.5.2.

The full scale hybrid control approach is demonstrated in Figure 4.2. The insect is brought from rest (Figure 4.2a) and into constant flapping by supplying a sequence of 3V, 25Hz DC pulses with a 50% duty cycle for 0.5 seconds followed by one second pauses, which are driven between the electrode in the antennal lobe and the common ground in the dorsal thorax (Figure 4.1b). Our electronic stimulus technique targets neuromuscular activity in the brain and dorsal thorax simultaneously. The result is that the pulses slow the moth down when the voltage is being supplied, but as pulses are relieved through the pre-programmed pause it prompts the insect into a fight or flight response and consequently strong flapping activity. After 30 seconds of sustained flight, the electronic pulses were stopped on command; which were followed by the actuation of the microfluidic chip. The delivery of a 5M solution of LGA leads to a paralytic effect [11] due to the overstimulation of the moth's nervous system through rapid depolarizations (rises in neuron membrane potential) [24]. The moth first responded first by decelerating 20 seconds after actuation, until it reached full

paralysis after 40 seconds (Figure 4.2c). The DC pulses routine resumed 80 seconds later, but the chemical paralysis completely overrides the applied electrical stimuli. Tracking of the moth's displacement using an indoor GPS system is shown in Figure 4.2d. Here it can be seen that moth's response to the electrical stimulation is evidenced by increased flapping activity and a sudden increase in flight altitude.

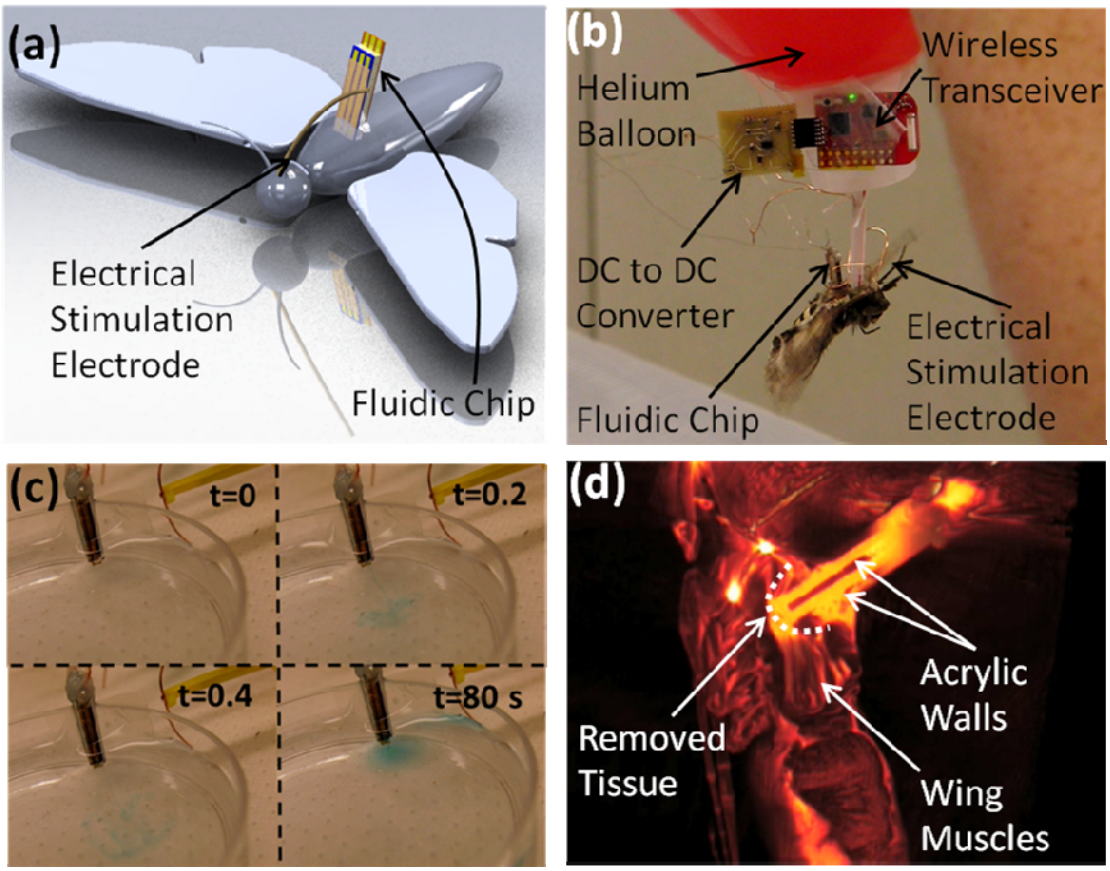

Figure 4.1. Device layout and operation. (a) Conceptual image of experimental setup showing the microfluidic chip which is implanted in dorsal thorax, and the copper wire used in electrical stimulation implanted in antennal lobe (b) Full scale experimental setup showing wireless transceiver and DC to DC converter. (c) Sample ejection sequence of 5M L-Glutamic acid solution into 10mM PBS solution. (d) 3D Computer Tomography image of fluidic chip implanted into dorsal thorax.

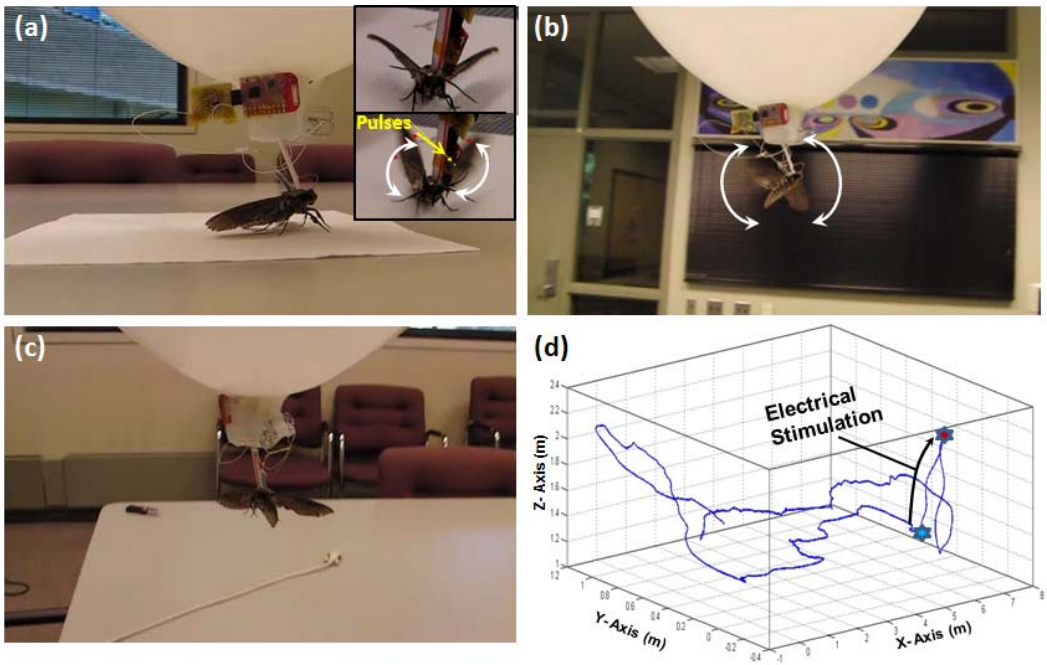

Figure 4.2. Full scale experimental setup. (a) Moth at rest. Inset shows how activity can be initiated from rest (top) to flapping (bottom) on command through applied DC pulses. (b) Electrical stimulation in mid air before fluidic chip actuation. (c) After dispensing 5M LGA solution leading to full paralysis. (d) Tracking displacements via indoor GPS system.

4.4 Chemical Override of Electrical Stimuli and Enhancing Flight Longevity

In our previous work [11], we show that it takes a Manduca Sexta moth over three hours to recover half of its wing flapping activity from a 15µl dose of 5M LGA. Because of this, here we focus on using electrical stimulation to enable quicker locomotive activity recovery from chemically induced paralysis. For these experiments, the moth was tethered to a hinged straw as shown in Figure 4.3a, and its displacement angle (activity) was measured and analyzed [25] as a function of LGA dose concentration for the same electrode setup and sequence of pulses described above. (Please refer to Materials and Methods Section 4.5.3 for more details on the angle experiments). Figure 4.3b shows a sample experiment, in which locomotive

activity first drops quickly after injecting 10μL of 0.5M LGA solution (dose volumes were kept constant across tests). Electrical stimulation is then initiated, and activity gradually increases with the aid of time and the supplied pulses. The observed oscillation in activity shown in this figure occurs due to the untargeted nature of the applied electrical stimuli; slowing the moth down (angle decrease) as the pulses are applied followed by strong flight during the shock recess. For concentrations 1M and below, most moths regained full post-injection activity nearly 10 minutes after LGA delivery as shown on Figure 4.3c, while those subjected to 5M doses regained half of their activity 1.5 hours later, which a twofold improvement from our previous work. The total activity for this time period and for each concentration is shown in Figure 4.3d, where moths subjected to smaller concentrations of LGA showed higher flapping activity in the first twenty minute interval. From these results, it is recommended to keep the dose concentration below 1M if quick reanimation is desired. Most importantly, just as the previous section showed how the applied chemical load can override the electrical stimuli, here electricity is supplied to overcome the chemical paralysis, showing that both approaches are synergistic.

Since Manduca Sexta moths fly sporadically (around 4 times a day and very sensitive to external environmental conditions [26]), it becomes necessary to override their neuromuscular activity to achieve controlled long term flight. We now use electrical stimuli to enhance their flight longevity, as is presented in Figure 4.4. Here moths were subjected to a setup similar to that explained in Figure 4.3, but without the chemical stimulants. For these experiments, two types of flyers were observed; a first group which managed to fly on the order 186 minutes on average while the others flew for 17 minutes on average. The criterion used in these experiments was that 10 seconds of no flapping activity is considered as a full stop and the end of a test. It can also be noted that even the lower flying group shows significantly more activity than

traditional moth flight behavior in terms of continuity and flight duration. The criterion used in these experiments was that 10 seconds of no flapping activity is considered as a full stop and the end of a test. It can also be noted that even the lower flying group shows significantly more activity than traditional moth flight behavior in terms of continuity and flight duration.

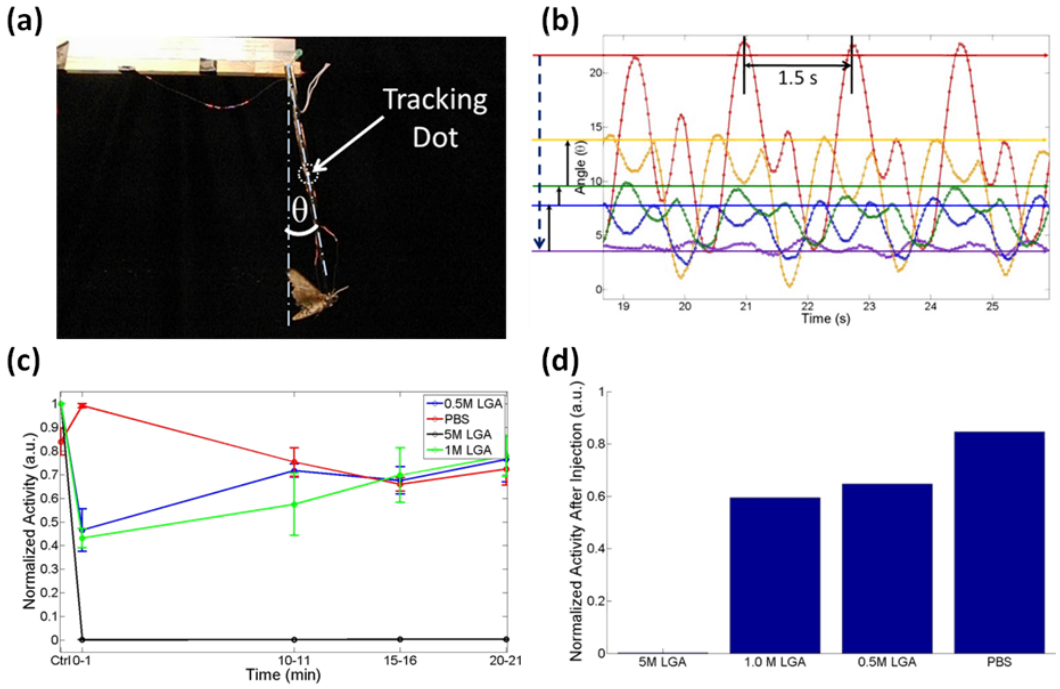

Figure 4.3. Electrical recovery from chemically induced paralysis. (a) Experimental setup showing moth attached to hinged straw. (b) Oscillation in mean angle due to untargeted nature of electrode setup; where DC pulses slow the moth down, followed by fight or flight response. (c) Normalized flapping activity as a function of dose and time. (d) Total activity for this time period, where higher doses of L-Glutamic acid doses lead to lower flying capability over the first 20 minutes.

.

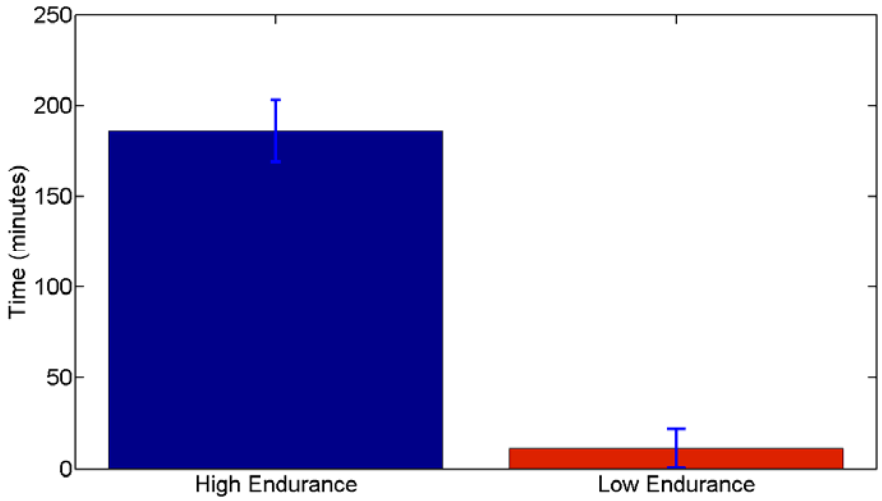

Figure 4.4. Enhancing flight endurance through electrical stimuli. Even low performing flyers demonstrated substantially better flying capability than moths not subjected to electrical excitation.

4.5 Materials and Methods

4.5.1: Microfluidic Device Fabrication and Assembly

Our drug delivery system consists of three subcomponents. The first is a silicon layer that contains a microwell with a suspended upper electrode through which fluids are ejected, a 3D printed acrylic channel coated with Parylene, and a bottom Pyrex substrate which contains the bottom counter electrode. The top silicon component was devised using the method established by Chung and Erickson [23], in which LPCVD silicon nitride is deposited on both sides of the <100> n-doped silicon wafer and the backside was patterned to define the well location, followed by gold deposition on the top side. The wells were then defined by immersing the wafer in KOH overnight and the remaining silicon nitride underneath the gold membrane was removed through reactive ion etching, leading to a square suspended gold membrane with 100 μm on its

side. A photoactive polyimide layer was spun and patterned on the top of the device to reduce electrical contact outside of the suspended god membrane. 1 mm tall acrylic channels were defined and cleaned with an NaOH solution, followed by a Parylene deposition to ensure impermeability to water. The three subcomponents were then assembled and sealed using Loctite 454: ISO 10993 since its fast curing and biocompatible. The assembled device was then subjected to oxygen plasma cleaning, and then the fluidic channel was filled with the chemical agents of interest, followed by a wax seal on the back of the device to ensure that no leakage occurs.

4.5.2: Microfluidic Chip and Copper Electrode Implantation

The microfluidic chips were implanted in adult moths 2 days after emerging from the pupal stage to ensure strong fliers. Prior to the surgery, the moths were placed on ice platform for approximately 10 minutes to lower internal body pressure and to minimize movement. With the use of a sterilized scalpel, the dorsal exoskeleton and body skin were removed and the chip was partially implanted 2mm into the thorax near the dorsolongitudinal flight muscles. After gently inserting the device into the thorax, the wound is sealed using Loctite 454: (ISO 10993). This step was followed by the thin copper electrode is implantation, which is gently inserted next to antennal lobe and sealed with the same biocompatible glue.

4.5.3: Angle Measurement and Longevity Experiments

The moth was tethered onto a straw via a chicken wire leash between its head and thorax. Electrodes were implanted using the same technique shown in Section 4.5.2, and the same electrical pulse setup (3V, 25Hz DC pulses with a 50% duty cycle for

0.5 seconds followed by one second pauses) was used to stimulate the moths into flapping. 10μL of solution was used across the chemical tests, and the displacement angle was evaluated using Herdick *et al.*'s.[25] MATLAB® software.

4.6 Acknowledgments

The authors would like to thank Justin Atchison for his contributions towards the boost converter design and implementation, Michael Kalontarov for helpful discussions, Prof. Hod Lipson for access to the 3-D Acrylic Printer and Dr. Mehmet Ozgur at the MEMS and Nanotechnology Exchange for backside etching process. This work was supported by the Defense Advanced Research Projects Agency Defense Sciences Office under the Hybrid Insect MEMS "HI-MEMS" program through the Boyce Thompson Institute for Plant Research. Distribution unlimited. Portions of this work were also supported by the Office of Naval Research under grant "Autonomous Microfluidic Devices for Battlefield Health Assessment and Treatment" which has award number N000141010115. The facilities used for this research include Nanoscale Science & Technology Facility (CNF), Nanobiotechnology Center (NBTC) at Cornell University.

4.7 Contributions

B.C. and A.J.C. were responsible for the device fabrication, electrical integration and running the bulk of the insect experiments and analyzing all the data. N.J. was in charge of programming the wireless microcontroller, X.T.H aided in the chemical characterization. B.C., A.J.C and D.E. were responsible for writing the paper. All authors discussed the results and commented on the manuscript.

REFERENCES

1. Wootton, R., *Aerodynamics: From insects to microvehicles.* Nature, 2000. **403**(6766): p. 144-145.
2. Bozkurt, A., R.F. Gilmour, and A. Lal, *Balloon-Assisted Flight of Radio-Controlled Insect Biobots.* Ieee Transactions on Biomedical Engineering, 2009. **56**(9): p. 2304-2307.
3. Bozkurt, A., R.F. Gilmour, A. Sinha, D. Stern, and A. Lal, *Insect-Machine Interface Based Neurocybernetics.* Ieee Transactions on Biomedical Engineering, 2009. **56**(6): p. 1727-1733.
4. Bozkurt, A., A. Lal, and R. Gilmour, *Aerial and terrestrial locomotion control of lift assisted insect biobots.* Conf Proc IEEE Eng Med Biol Soc, 2009. **2009**: p. 2058-61.
5. Sato, H., C.W. Berry, Y. Peeri, E. Baghoomian, B.E. Casey, G. Lavella, J.M. Vandenbrooks, J.F. Harrison, and M.M. Maharbiz, *Remote radio control of insect flight.* Front Integr Neurosci, 2009. **3**: p. 24.
6. Tsang, W.M., A.L. Stone, Z.N. Aldworth, J.G. Hildebrand, T.L. Daniel, A.I. Akinwande, and J. Voldman, *Flexible Split-Ring Electrode for Insect Flight Biasing Using Multisite Neural Stimulation.* Ieee Transactions on Biomedical Engineering, 2010. **57**(7): p. 1757-1764.
7. Daly, D.C., P.P. Mercier, M. Bhardwaj, A.L. Stone, Z.N. Aldworth, T.L. Daniel, J. Voldman, J.G. Hildebrand, and A.P. Chandrakasan, *A Pulsed UWB Receiver SoC for Insect Motion Control.* Ieee Journal of Solid-State Circuits, 2010. **45**(1): p. 153-166.

8. Lian, Y.S., W. Shyy, D. Viieru, and B.N. Zhang, *Membrane wing aerodynamics for micro air vehicles.* Progress in Aerospace Sciences, 2003. **39**(6-7): p. 425-465.

9. Jeon, Y.B., R. Sood, J.h. Jeong, and S.G. Kim, *MEMS power generator with transverse mode thin film PZT.* Sensors and Actuators A: Physical, 2005. **122**(1): p. 16-22.

10. Wickenheiser, A.M., T. Reissman, W.J. Wu, and E. Garcia, *Modeling the Effects of Electromechanical Coupling on Energy Storage Through Piezoelectric Energy Harvesting.* Ieee-Asme Transactions on Mechatronics, 2010. **15**(3): p. 400-411.

11. Chung, A.J. and D. Erickson, *Engineering insect flight metabolics using immature stage implanted microfluidics.* Lab on a Chip, 2009. **9**(5): p. 669-676.

12. Tanaka, M., *An industrial and applied review of new MEMS devices features.* Microelectronic Engineering, 2007. **84**(5-8): p. 1341-1344.

13. Franz, M.O. and H.A. Mallot, *Biomimetic robot navigation.* Robotics and Autonomous Systems, 2000. **30**(1-2): p. 133-153.

14. Wood, R.J., *The first takeoff of a biologically inspired at-scale robotic insect.* Ieee Transactions on Robotics, 2008. **24**(2): p. 341-347.

15. Ellington, C.P., *The Aerodynamics of Hovering Insect Flight .1. the Quasi-Steady Analysis.* Philosophical Transactions of the Royal Society of London Series B-Biological Sciences, 1984. **305**(1122): p. 1-15.

16. Pesavento, U. and Z.J. Wang, *Flapping Wing Flight Can Save Aerodynamic Power Compared to Steady Flight.* Physical Review Letters, 2009. **103**(11).

17. Helm, B., *Finding Land Mines by Following a Bee*, in *Business Week*. 2005.

18. Weinberger, S., *Defence research: Still in the lead?* Nature, 2008. **451**: p. 390-393.

19. Ziegler, R. and M. Schulz, *Regulation of Carbohydrate-Metabolism During Flight in Manduca-Sexta.* Journal of Insect Physiology, 1986. **32**(12): p. 997-1001.

20. Ziegler, R., *Changes in Lipid and Carbohydrate-Metabolism During Starvation in Adult Manduca-Sexta.* Journal of Comparative Physiology B-Biochemical Systemic and Environmental Physiology, 1991. **161**(2): p. 125-131.

21. Claassen, D.E. and A.E. Kammer, *Effects of Octopamine, Dopamine, and Serotonin on Production of Flight Motor Output by Thoracic Ganglia of Manduca-Sexta.* Journal of Neurobiology, 1986. **17**(1): p. 1-14.

22. Johnston, R.M. and R.B. Levine, *Crawling motor patterns induced by pilocarpine in isolated larval nerve cords of Manduca sexta.* Journal of Neurophysiology, 1996. **76**(5): p. 3178-3195.

23. Chung, A., Y. Huh, and D. Erickson, *A robust, electrochemically driven microwell drug delivery system for controlled vasopressin release.* Biomedical Microdevices, 2009. **11**(4): p. 861-867.

24. Skinner, W.S., P.A. Dennis, J.P. Li, R.M. Summerfelt, R.L. Carney, and G.B. Quistad, *Isolation and Identification of Paralytic Peptides from Hemolymph of the Lepidopteran Insects Manduca-Sexta, Spodoptera-Exigua, and Heliothis-Virescens.* Journal of Biological Chemistry, 1991. **266**(20): p. 12873-12877.

25. Hedrick, T.L., *Software techniques for two- and three-dimensional kinematic measurements of biological and biomimetic systems.* Bioinspiration & Biomimetics, 2008. **3**(3).

26. McCrea, M.J. and J.E. Heath, *Dependence of Flight on Temperature Regulation in Moth, Manduca-Sexta.* Journal of Experimental Biology, 1971. **54**(2): p. 415.

CHAPTER 5

A NOVEL POLYMER MICRONEEDLE FABRICATION PROCESS FOR ACTIVE FLUIDIC DELIVERY*

5.1 Abstract

In this paper, we explore a new fabrication process for a flexible, all polymer, active fluidic delivery system, incorporating a fusion of laser micromachining and microfabrication techniques as well as rapid prototyping technology. Here we show selective fluidic delivery from isolated microchannels through an electrochemically driven pumping reaction, demonstrate the dispensing of dose volumes up to 5.5 μL, and evaluate the device's performance in terms of its delivery speed and ejection efficiency. Finally, we move this work towards an implantable microfluidic drug delivery device by investigating the device's biocompatibility through a statistical approach that overviews the viability of bovine aortic endothelial cells on polyimide and silicon substrates.

* Re-printed with kind permission from Springer Science Business Media: Cordovez, B., Chung, A.J., Mak, M., Erickson, D., "A Novel Polymer Microneedle Fabrication Process for Active Fluidic Delivery" *Journal of Microfluidics and Nanofluidics*. **s**10404-010-0709-x (2010) . The original publication is available at www.springerlink.com

5.2 Introduction

Advancements in implantable drug delivery systems have enabled the transition from passive delivery to active schemes. While passives technologies [1-4] are characterized by immediate drug release upon insertion or ingestion and are generally driven by diffusive transport, active control [5-9] provides the ability to localize drug delivery with microscopic precision, direct the timing of release, and control the rate of release. These systems have been used in applications ranging from potential medical uses including hemorrhagic shock prevention through rapid vasopressin delivery [8], polypeptide delivery for therapeutics [5], controlled anti epileptic drug release [10], angiogenesis control [11], to on command chemically induced paralysis of live micro-air vehicles [9].

Polymer micro-needles are of interest for implantable drug delivery due to their enhanced biocompatibility [12], and capability to conform to tissue without shattering during the insertion or tissue reconfiguration processes [13]. These devices have been fabricated using several polymers including polydimethylsiloxane (PDMS) [14, 15], polylactic and polyglycolic acid (PLGA) [13, 16], block copolymer hydrogels [17] SU-8 photoresist [18] and polyimide [19, 20]. Among these, polyimide is particularly useful due to its electrical and thermal insulation properties as well as its capability to be patterned directly through microfabrication. To date however most polymer based drug delivery devices have either relied upon passive schemes as discussed above, or employ complicated and not easily integratable active delivery methods like peristaltic pumping through piezo-electrics [13], large peristaltic pumps [15] and syringe pumps [19, 20].

In this paper, we present a device that incorporates the flexibility and biocompatibility of polymer microneedles while still offering the advantages of active

drug delivery devices in a simple microfluidic architecture. Our device uses a similar electrochemical release and dose control mechanism as our previous work [8] but is now integrated into a flexible system as opposed to its silicon predecessor. In this paper we present our fabrication methodology and electrochemical ejection performance. Furthermore, we illustrate the device's ability to selectively dispense from different electrochemical chambers and also provide an assessment of the system's enhanced biocompatibility by analyzing the viability of bovine aortic endothelial cells on our polyimide surfaces in comparison with silicon substrates.

5.3 Flexible Electrochemical Drug Delivery

5.3.1: Device Layout and Operation

Figure 5.1a illustrates the device constituents and assembly procedure. Briefly, the device assembly consists of a top 250 μm thick double sided polished polyimide substrate which hosts a gold electrode and a 400 μm^2 suspended gold membrane. The fluid contents are stored in 3D printed acrylic channels which can store up to 15μL of solution, and the system is closed by a bottom polyimide component which contains a counter gold electrode. As will be detailed in the next paragraph, the fluidic contents will burst through the gold membrane and into the chip's exterior through an electrochemical reaction generated by applying an electric potential between the top and bottom electrodes. Figure 5.1b shows a fully assembled two- channel flexible microfluidic needle. A cross section image of the top polyimide device fabrication procedure after the laser etching, dry etching, and chrome wet etch steps which result in suspended gold membranes roughly 400 square microns in size is presented in Figure 5.1c. Unlike our previous silicon based devices [8, 9], our new architecture is

fully flexible as presented in Figure 5.1d, and has the ability to adapt to tissue effectively for localized delivery. Furthermore, the new flexible version can contain up to four individually addressable fluidic channels which contain the same amount of pay load in each channel as its previous single chamber silicon counterpart for the same device geometry.

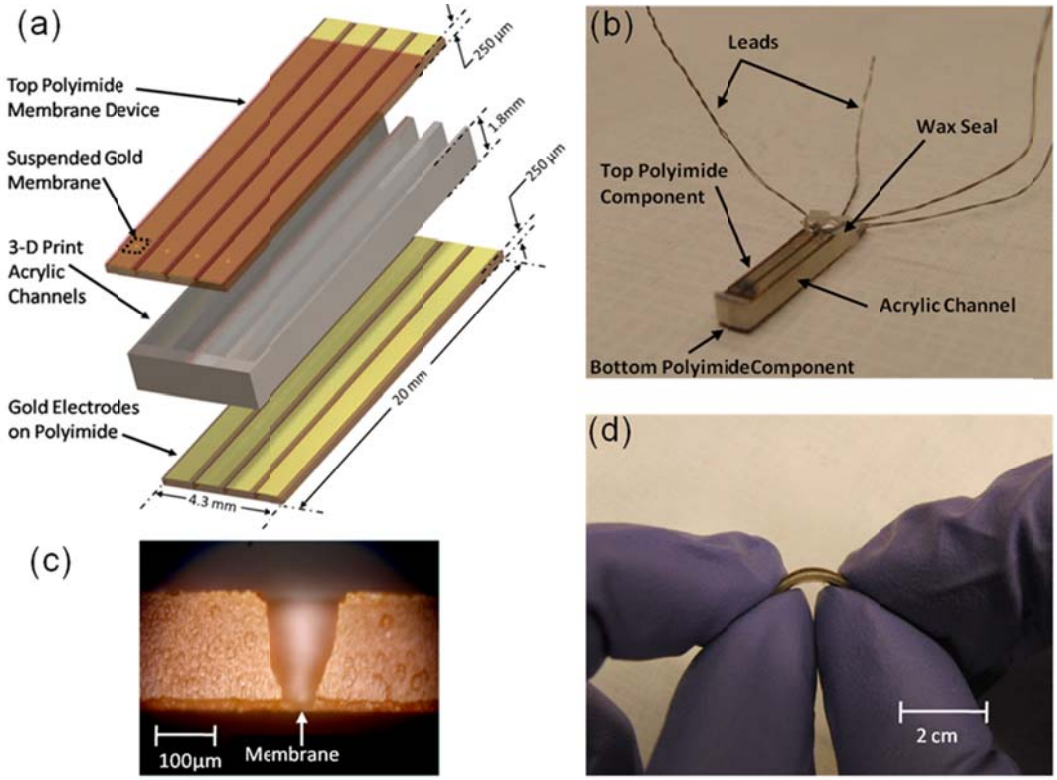

Figure 5.1. Device Layout and Assembly. (a) Schematic of the device subcomponents and assembly procedure. (b) A two channel flexible electrochemical needle. (c) Suspended gold membrane fabrication procedure after the laser etching, dry etching, and chrome wet etch steps. (d) Device in bending.

Figure 5.2 shows a time-lapse of images of the electrochemical ejection procedure. The basic electrochemical pumping operation procedure was established in our previous publication [8] and by Santini *et al.* [6], but briefly the drug delivery system

works by a two phase electrochemical reaction driven between the capping gold membrane and the bottom electrode located inside the reservoir. First, the electrolytic component of the reaction builds up the pressure in the closed fluidic system due to electrolysis (*i.e.* as gas bubbles are formed in the closed channel, the pressure in the chamber builds up). In addition, at the anode, chlorine ions in the buffer solution react with the gold membrane to form a water soluble chlorogold complex that degrades it as the reaction proceeds until it ruptures and opens. Finally, the pressure is relieved by ejecting the fluidic contents to the chip's exterior. After applying a 30 V potential for 40 seconds, gold dissolution occurring in the state that we note as t=0 (Figure 5.2a). The fluidic ejection procedure 1.6 and 3.2 seconds later is shown in Figures 5.2b and 5.2c, respectively in which the PBS solution containing 50 nm fluorescent polystyrene microspheres. The ejection flow rate rapidly increases from t = 5 seconds (Figure 5.2d) onwards, dispensing nearly 3 µL of solution out of the well in over the course of two minutes. Right after the onset of rupture, the ejection procedure becomes more rapid as the membrane aperture size increases. Though usually uniform, we did notice that fluid ejection to the outside environment can occur in spurts.

Figure 5.3 displays the mean ejection volume as a function of time for experiments operated at a 30V potential. This high potential was chosen since it was previously found that the fluid ejection rate maps to electric potential almost linearly [7, 8]. For these conditions, on average 17% of the contents managed to eject out of the system after 2 minutes. In most experiments, the delivery rate is highest for the first 30s following rupture (dispensing at ~ 0.1 µL/s) and decays with time. Though the general trend agrees with our previous publications, in the best of cases only 37% of the fluids (5.5 µL) managed to leave the polyimide devices, less than its previous silicon counterpart. Electrolysis not only contributes to the increase in pressure, but

unfortunately the formed gas bubbles can also block the main fluidic channel (acrylic) and the inverted channel (polyimide) that leads to the suspended membrane.

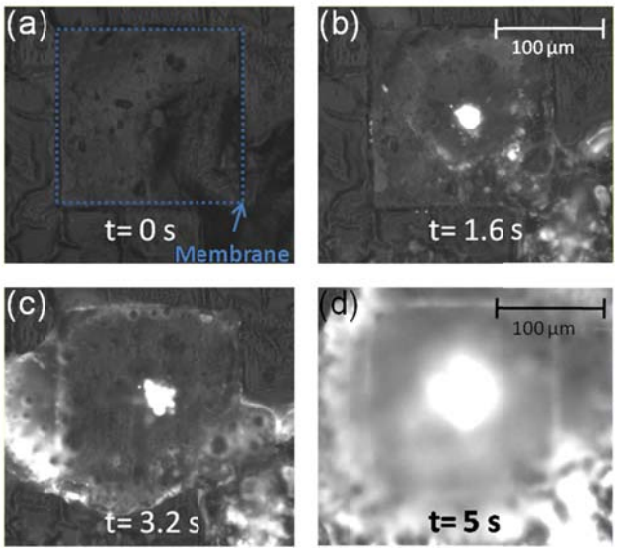

Figure 5.2. Electrochemical Ejection Procedure. (a) Prior to membrane rupture and 40 seconds after first applying electric potential. (b) Fluidic ejection 1.6 seconds and (c) 3.2 seconds after the onset of gold membrane rupture. (d) Increased flow rate after 5 seconds from membrane rupture.

Furthermore, large gas bubbles can disconnect the liquid stream and generate an adverse pressure gradient, keeping much the liquid contents from leaving the chip. In our next generation of needles, the laser micromachining etch area will be wider in order to increase the membrane aperture and enable a higher rate of delivery, and the use of gas permeable materials will be investigated to mitigate the clogging behavior. It should be noted that the mean current during ejection was 0.2 mA, thus the system consumes an average power of 6 mW, which is still very low compared to traditional autonomous delivery devices [21-23].

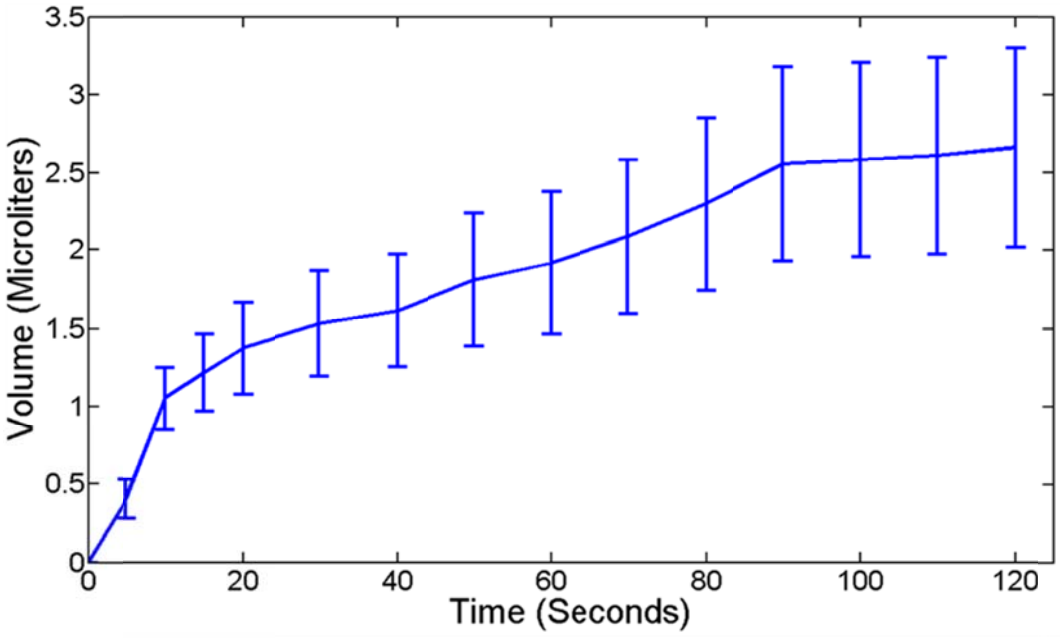

Figure 5.3. Device ejection volume performance results at 30V.

5.3.2: Fluidic Channel Addressing

Figure 5.4 displays a multi-chamber device with independent multiplexing capability. Figure 5.4a shows the selective fluidic actuation of the bottom channel in a 2 needle setup 41 seconds after ejection, and Figure 5.4b shows the ability to actuate the top channel (123 seconds later), with little to no cross talk between channels. There is only a potential applied to the top channel in Figure 5.4b, and the smaller ejection volume evidenced in the bottom channel is due to fluid evaporation and creeping back into the reservoir. We did observe fluidic cross talk when liquid surfaces from different channels coalesce; or after 4 minutes (roughly) after the electrolytic reaction starts to dissolve the epoxy adhesive that binds the polyimide substrates to the acrylic, making underflow leakage possible. This problem can be reduced by using wider acrylic channels since it will take longer to dissolve the majority of the biocompatible epoxy.

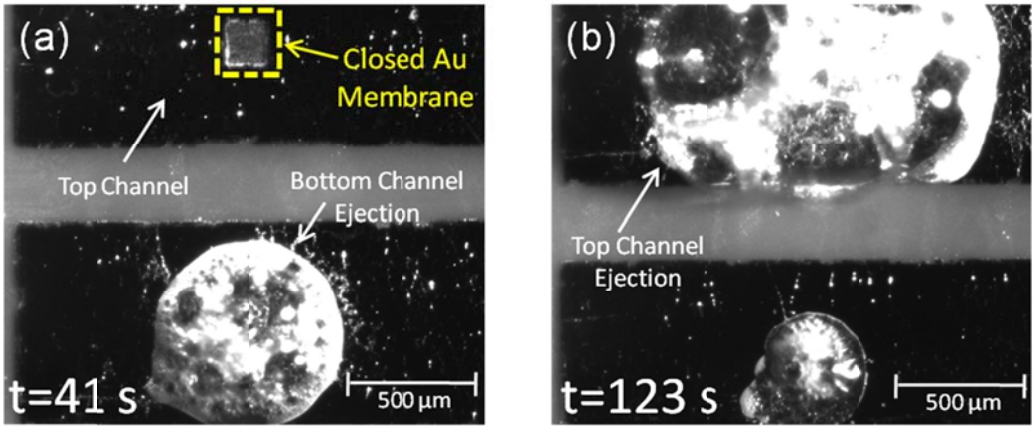

Figure 5.4. Fluidic Channel Multiplexing. (a) Bottom channel actuation 41 seconds after ejection. (b) Top channel addressing 123 seconds after the onset of rupture.

5.3.3: Biocompatibility of Silicon and Polyimde Needles: A Comparison

In Section 5.3 we demonstrated the high degree of flexibility of all polymer needle device and we now investigate whether polyimide it is at least as biocompatible as silicon; which is the most common substrate for current implantable micro-devices [6] and our previous material of choice [8]. In this section we analyze the biocompatibility of our devices using bovine aortic endothelial cells as our control biology. For more details on the cell seeding procedure, please refer to the Fabrication and Methods Section. For each substrate (polyimide and silicon), cells were seeded onto the surface and submerged inside a petridish filled with cell culture media. On each of the specified days, living cells that were adherent to the substrate surface and were imaged on an upright microscope, counted, and averaged over 10 different regions, as shown in Figure 5.5. Cells on the petridish surface containing one of those substrates were also counted and averaged on day 7. The areas of all regions used were the same. The average concentration on each substrate on days 2, 4, and 7 was normalized by the average concentration of cells on the petridish on day 7, and the results are shown on

Figure 5.6a. The initial concentration (on day 2) on the silicon substrate was higher than that on polyimide, but in the course of one week, cell viability decreased for both, and the rate of decrease appears higher for silicon. A similar fraction of cells were found on both substrates on day 4, and very few cells survive for over one week as evidenced by Figure 5.6b. The cell viability is comparable for silicon and polyimide, but notice particularly that the fraction of remaining cells is much higher for polyimide, and thus is likely to be a better substrate for implantation.

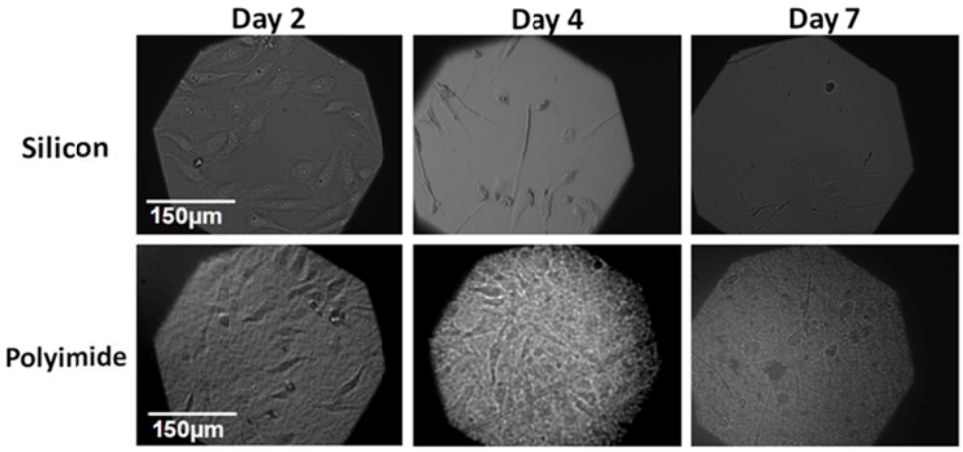

Figure 5.5. Cell Viability as a Function of Substrate and Time: Viability analysis of bovine aortic endothelial cells in polyimide and silicon substrates in Days 2, 4 and 7.

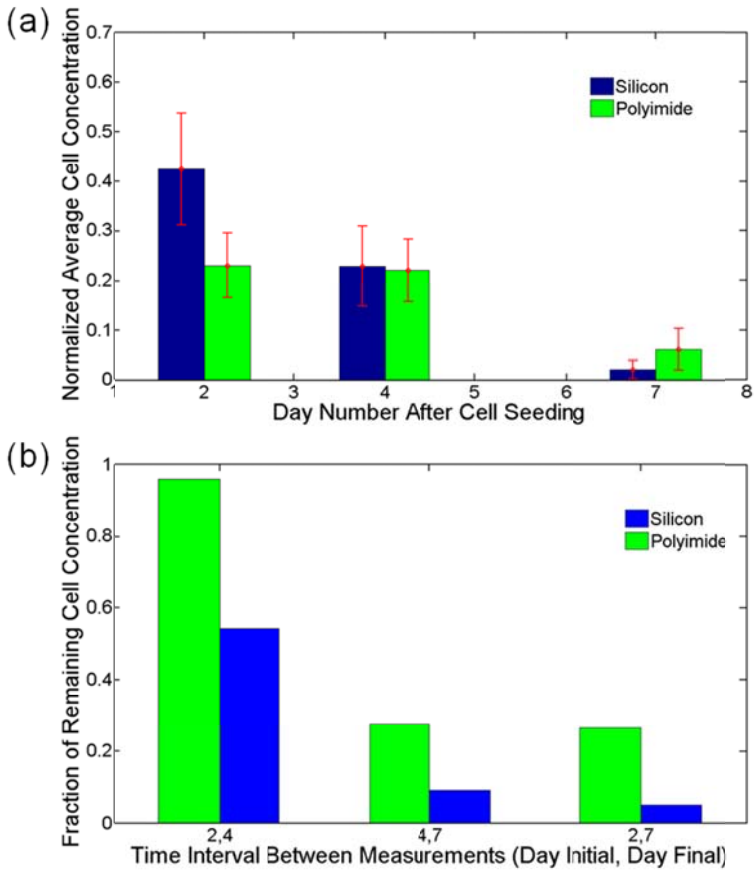

Figure 5.6. Biocompatibility of Polyimide and Silicon Needles: (a) Normalized average cell concentration on each substrate on days 2, 4, and 7. (b) Fractional decrease in cell concentration between reference days.

5.4 Fabrication and Methods

5.4.1: Top Substrate Fabrication

The substrate used is a double side polished, 250 µm thick polyimide substrate. The top was patterned through gold liftoff via a chrome adhesion layer that also serves as an etch stop, and an aluminum etch mask at the bottom which define the blind hole laser etch locations. The majority of the backside etch (~240 µm) was performed

through a deep laser etch, which yielded a mean etch angle of 10 degrees with the vertical. Due to heating during this etching procedure, this step was hard to control is resulted in irregular final membrane dimensions varying from 125 μm^2 to 650 μm^2 The dry etching step was finished using a 70% 0_2, 30% CF_4 etch 250W RIE power, with the role of CF_4 being that of etching inorganics found in the polyimide [24], enabling a quicker etch. The aluminum mask layer was removed via a wet etch. At this point, the top of the gold layer was insulated with the exception of the membrane location using a 2 μm thick photoactive polyimide, to minimize electrical interaction with the surroundings. We then wet etched the remaining chrome layer, yielding roughly a 400 μm^2 (on average) suspended gold membrane. The backside of this polyimide channel was then subjected to an oxygen plasma clean to ensure wettability of the substrate.

5.4.2: Acrylic Channel Fabrication and Softening

Channels holding ~15 μL of solution (2mm tall and 750 μm wide), were fabricated by 3D printing of acrylic. The defined structures were then left in 2% NaOH for 60 hours, which served to remove any sacrificial material remaining from the printing procedure, as well as permeate through the porous acrylic channels, making the resulting structure flexible. To make the structure water impermeable, we deposited 2 μm of parylene conformally around the channels.

5.4.3: Bottom Electrode Substarte

The bottom gold electrode was also defined on a 250 μm thick polyimide substrate through liftoff and also uses a chrome adhesion layer. Single electrodes were diced

using a laser cutter (or alternatively a scalpel). As on the top electrode, platinum contacts were placed in electrical contact with the gold through silver conductive epoxy.

5.4.4: Needle Assembly

After plasma treating the bottom of the top substrate to ensure that liquid fills the etched cavity that leads to the suspended gold electrode, the acrylic channels were bonded to the top and bottom polyimide by dipping the acrylic channels on a pre-spun glass slide containing Loctite 405® adhesive. The polyimide and acrylic pieces were then aligned and left to bond for 24 hrs. The channels were then filled from the back with 10mM PBS solution, and this part of the structure was sealed with 5 minute quick dry epoxy.

5.4.5: Cell Culture and Biocompatibility Experiment Setup

Bovine aortic endothelial cells were used for these experiments. They were fed with Leibovitz L-15 media and incubated at 37^{o}C and 0% CO_2. Media were replenished every day. For the experiment, one strip of silicon and one polyimide device were used as substrates for a viability comparison assay. Prior through usage, each strip was sterilized with 70% isopropanol 30% water and dried off completely. Each was placed in the bottom of separate petridishes and submerged in 2 mL of Leibovitz L-15 media, and 350 cells/mm^2, suspended through trypsinization, were then seeded in each petridish. The images shown in Figure 5 recorded on days 2, 4, and 7 after initial cell seeding.

5.5 Discussion and Conclusions

Though effective fluid ejection was consistently demonstrated here, in some cases the ejection rate tended to be irregular. This ejection irregularity is likely due to gas bubbles generated through the electrolytic procedure that clogging the main fluidic channel (acrylic) and the inverted channel (polyimide) that leads to the suspended membrane. We believe that this effect also plays an important role on the overall device performance; since large gas pockets can disconnect the liquid stream and in turn generate an adverse pressure gradient, hindering the remaining fluid from leaving the chip's interior. Furthermore, since the inverted polyimide channel that leads to the membrane is narrower than that of our previous silicon based device (see Fabrication and Methods Section), gas bubble induced clogging is more likely to occur compared to our previous approach. It is also important to note that when comparing the rupture initiation time to our previous results [8], the polyimide based device takes roughly 25% longer to initiate ejection since our exposed membrane has a shorter span and is thus more stiff and has a smaller area for dissolution. In future devices, the laser etch area will be wider in order to enable an increase the dose delivery rate through a larger membrane aperture. Though there is a degradation in performance due to gas bubble formation, it is important to note that this chip does manage to perform both controlled and highly localized delivery in a flexible and biocompatible substrate in a small and easily implantable architecture.

The multiplexing capability demonstrated by this chip does enable one to deliver different concentrations and types of chemicals [6]. Furthermore, multiple channels also provide redundancy in the case of faulty post- insertion membranes, which could be damaged useful in overcrowded insertion regions. In terms of the cross channel leakage mentioned above, it takes approximately 4 minutes for the electrolytic

reaction to dissolve the binding epoxy, placing an upper limit on the time for delivery. This time could be improved by using wider channels to prevent underflow leakage, though it would come at the expense of a larger device. In terms of the device's biocompatibility, we conclude that cell viability, which is our measure of biocompatibility here, is comparable for silicon and polyimide, but particularly that the rate of decrease in cells appears higher for the silicon.

5.6 Acknowledgments

The authors would like to thank Michael Kalontarov for helpful discussions, Prof. Hod Lipson for access to the 3-D Acrylic Printer and Dr. Mehmet Ozgur at the MEMS and Nanotechnology Exchange for the laser etch process. This work was supported by the Defense Advanced Research Projects Agency Defense Sciences Office under the Hybrid Insect MEMS "HI-MEMS" program through the Boyce Thompson Institute for Plant Research. Distribution unlimited. Portions of this work were also supported by the Office of Naval Research under grant "Autonomous Microfluidic Devices for Battlefield Health Assessment and Treatment" which has award number N000141010115. The facilities used for this research include Nanoscale Science & Technology Facility (CNF), Nanobiotechnology Center (NBTC) at Cornell University.

REFERENCES

1. Ahmed, A., C. Bonner, and T.A. Desai, *Bioadhesive microdevices with multiple reservoirs: a new platform for oral drug delivery.* Journal of Controlled Release, 2002. **81**(3): p. 291-306.
2. Grayson, A.C.R., M.J. Cima, and R. Langer, *Size and temperature effects on poly(lactic-co-glycolic acid) degradation and microreservoir device performance.* Biomaterials, 2005. **26**(14): p. 2137-2145.
3. Ainslie, K.M. and T.A. Desai, *Microfabricated implants for applications in therapeutic delivery, tissue engineering, and biosensing.* Lab on a Chip, 2008. **8**(11): p. 1864-1878.
4. Kristy, M.A., D.L. Rachel, T.B. Tristan, P. Lamar, M.B. Eric, and A.D. Tejal, *Microfabricated Devices for Enhanced Bioadhesive Drug Delivery: Attachment to and Small-Molecule Release Through a Cell Monolayer Under Flow.* Small, 2009. **5**(24): p. 2857-2863.
5. Prescott, J.H., S. Lipka, S. Baldwin, N.F. Sheppard, J.M. Maloney, J. Coppeta, B. Yomtov, M.A. Staples, and J.T. Santini, *Chronic, programmed polypeptide delivery from an implanted, multireservoir microchip device.* Nat Biotech, 2006. **24**(4): p. 437-438.
6. Santini, J.T., M.J. Cima, and R. Langer, *A controlled-release microchip.* Nature, 1999. **397**(6717): p. 335-338.
7. Chung, A.J., D. Kim, and D. Erickson, *Electrokinetic microfluidic devices for rapid, low power drug delivery in autonomous microsystems.* Lab on a Chip, 2008. **8**(2): p. 330-338.

8. Chung, A., Y. Huh, and D. Erickson, *A robust, electrochemically driven microwell drug delivery system for controlled vasopressin release.* Biomedical Microdevices, 2009. **11**(4): p. 861-867.
9. Chung, A.J. and D. Erickson, *Engineering insect flight metabolics using immature stage implanted microfluidics.* Lab on a Chip, 2009. **9**(5): p. 669-676.
10. Huang, W.C., S.H. Hu, K.H. Liu, S.Y. Chen, and D.M. Liu, *A flexible drug delivery chip for the magnetically-control led release of anti-epileptic drugs.* Journal of Controlled Release, 2009. **139**(3): p. 221-228.
11. Cao, Y.H. and R. Langer, *Optimizing the Delivery of Cancer Drugs that Block Angiogenesis.* Science Translational Medicine, 2010. **2**(15).
12. Richardson Jr, R.R., J.A. Miller, and W.M. Reichert, *Polyimides as biomaterials: preliminary biocompatibility testing.* Biomaterials, 1993. **14**(8): p. 627-635.
13. Aoyagi, S., H. Izumi, and M. Fukuda, *Biodegradable polymer needle with various tip angles and consideration on insertion mechanism of mosquito's proboscis.* Sensors and Actuators A: Physical, 2008. **143**(1): p. 20-28.
14. Han-Kuan Anthony, T., A.M. Elizabeth, D. Sylvia, M. Marc, and K. Lawrence, *Integrating Biosensors and Drug Delivery: A Step Closer Toward Scalable Responsive Drug-Delivery Systems.* Advanced Materials, 2009. **21**(6): p. 656-660.
15. Chen, J., M. Chu, K. Koulajian, X. Wu, A. Giacca, and Y. Sun, *A monolithic polymeric microdevice for pH-responsive drug delivery.* Biomedical Microdevices, 2009. **11**(6): p. 1251-1257.

16. Park, J.-H., M.G. Allen, and M.R. Prausnitz, *Biodegradable polymer microneedles: Fabrication, mechanics and transdermal drug delivery.* Journal of Controlled Release, 2005. **104**(1): p. 51-66.

17. Morishita, M., T. Goto, K. Nakamura, A.M. Lowman, K. Takayama, and N.A. Peppas, *Novel oral insulin delivery systems based on complexation polymer hydrogels: Single and multiple administration studies in type 1 and 2 diabetic rats.* Journal of Controlled Release, 2006. **110**(3): p. 587-594.

18. Ane, A., G. Gemma, M.D.L.P. Liset, T. María, G. Anton, B. Javier, S. Rafa, V. Rosa, and L.J. Fernández, *SU-8-based microneedles for in vitro neural applications.* Journal of Micromechanics and Microengineering, 2010. **20**(6): p. 064014.

19. Metz, S., A. Bertsch, D. Bertrand, and P. Renaud, *Flexible polyimide probes with microelectrodes and embedded microfluidic channels for simultaneous drug delivery and multi-channel monitoring of bioelectric activity.* Biosensors and Bioelectronics, 2004. **19**(10): p. 1309-1318.

20. Ichimori, S., K. Nishida, S. Shimoda, T. Sekigami, Y. Matsuo, K. Ichinose, M. Shichiri, M. Sakakida, and E. Araki, *Development of a highly responsive needle-type glucose sensor using polyimide for a wearable artificial endocrine pancreas.* Journal of Artificial Organs, 2006. **9**(2): p. 105-113.

21. Zahn, J.D., A. deshmukh, A.P. Pisano, and D. Liepmann, *Continuous On-Chip Micropumping for Microneedle Enhanced Drug Delivery.* Biomedical Microdevices, 2004. **6**(3): p. 183-190.

22. Schomburg, W.K. and et al., *Assembly for micromechanics and LIGA.* Journal of Micromechanics and Microengineering, 1995. **5**(2): p. 57.

23. Jang, J. and S.S. Lee, *Theoretical and experimental study of MHD (magnetohydrodynamic) micropump.* Sensors and Actuators A: Physical, 2000. **80**(1): p. 84-89.

24. Popova, K., E. Spassova, I. Zhivkov, and G. Danev, *Reactive ion etching of vapor phase deposited polyimide films in CF4/O2: effect on surface morphology.* Thin Solid Films, 1996. **274**(1-2): p. 31-34.

CHAPTER 6

CONCLUSIONS

I was able to develop a reconfigurable microfluidic architecture that brings new frontiers in performance and functionality for microfluidics in biomolecule trapping, microfluidic storage and drug delivery applications. Below, I present the summary of my research accomplishments and contributions by project:

6.1 Summary of Individual Accomplishments by Project

6.1a: Electroactive Microwells

- Trapping 4 orders of magnitude faster compared to passive attraction schemes [1] for particles of the same size.
- Strong trapping potentials, up 5 orders of magnitude greater than the ambient thermal (Brownian) energy.
- Reversible particle trapping, which can be very useful for target probing and disposing in screening systems.
- Single step fabrication process.
- Predictable flow patterns through FEA Simulations that couple fluid and electrical forces.

6.1b: Optofluidic Data Storage

- Readout of up to 6-Bits of information in single diffraction 200nm (Blu-Ray®) [2] data sites.

    - Highest volumetric storage in fluid medium to date, which is 6 orders of magnitude greater in storage density than current microfluidic memories.
    - A geometric increase in storage density over current single layer optical storage media.

- Enabled non-volatile (no applied external power) storage through the use of an mediating agarose layer.
- Showed that different sized electroactive wells can be used for visual display and storage/detection purposes respectively.

6.1c: Hybrid Control of Insect Cyborgs

- First time wireless integration of chemical and electrical stimulation mechanisms for living insect micro air vehicle control.
- First time demonstration of microfluidic systems for chemical control of untethered insect micro air vehicles.
- Characterization of performance, recovery and endurance times of insects subjected to hybrid chemical and electrical stimulations.

6.1d: Active Drug Delivery Control through Flexible Polymer Microneedles

- Devised flexible and all polymer drug delivery needles capable of ejecting volumes up to 5.5 μL of solution.
- Fourfold reduction of silicon predecessor chip dimensions, while still enabling the same fluidic payload capacity.
- Multiple chamber capability provides the ability to deliver various chemicals and doses on demand with highly localized concentrations in targeted sub-millimeter dimensions.

6.2 Future Directions

Given the versatile and useful nature of my work on electroactive wells, my work has opened many doors. Below, I list some of the future directions my work could take by project:

6.2a: Electroactive Microwells

- Use this work directly for fast DNA and cell (a better spatial match for microwell geometries) microarray technology: Though there are commercial platforms (such as that owned by Gamida Inc. [3]) that can perform this work, my work provides a simpler and cheaper platform that enables more localized and targeted delivery. This would first involve determining the physiological implications of performing the trapping in direct current conditions, and continuously monitoring the environment via pH and temperature measurements, which leads to the integration of sensors inside the microwells.
- Integrate active sensors on wells: So far, I have used external measurement sources (fluorescence and spectrometry) to detect trapped particles in the well locations. However, since my device allows for high electric field localization,

it makes for a great host for an Impedance Based Sensing. [4]. These sensors could be integrated in situ to determine a biomolecule's size and its dielectric properties. If this specimen is not desired, it could be rejected from the well or even killed through localized joule heating.

- Electroactive wells can also aid sensing applications by both concentrating and mixing analyte in targeted locations. My colleagues and I used this process[5] to accumulate gold nanoparticles immobilized with DNA capture probes inside the electroactive microwells, and used the reversible electrokinetic process to mix these gold functionalized capture probes with Dengue virus (DENV-2a) DNA strands. Thought the sensing operation is outside the scope of this thesis, briefly the gold nanoparticles serve to increasing the Ramann scattering signal through Surface Plasmon amplification [6] in a Surface Enhanced Raman Scattering [7] (SERS) setup.

6.2b: Optofluidic Data Storage

- Synthesis: With the current advancements in Q-Dot synthesis technology [8] the storage density achieved can continuously increase every year.
- Protein nanoarray technologies: Humans have between 30,000 and 40,000 genes [9], but the number of combinations increases exponentially in the protein world. If an all inclusive protein microarray is envisioned, this work could help sense multiple proteins in a very compact and fast architecture.
- Information archiving: Since nanoparticle trapping and detection demonstrated by my work took roughly 200ms, this architecture could be used in situations in which density and not speed are of the essence, such as archiving.

- Full integration: More work still needs to be done to either integrate and/or generate a fully commercial device, with particular focus in enhancing speed and performance. Also, better avenues to reduce irreversible Q-Dot adhesion to base of wells should be pursued.

6.2c: Hybrid Control of Insect Cyborgs

- Chemical Excitation: Find adequate drugs for chemical excitation of moths and fully demonstrate that chemistry can be used effectively to stimulate and enhance moth flapping performance in addition to the aforementioned demonstrated paralysis. Octopamine [10] and Pilocarpine [11] are good candidates.
- Perform midflight nourishment experiments and investigated whether it allows it to fly and/or live longer.
- Make smaller components to enable more compact integration: This will allow our device to be incorporated with the other functionalities from the different HI-MEMS project [12] and generate a fully functional insect cyborg.
- With the smaller implants, move back to early pupal stage implantation microfluidics to enable better chip adaptation with the moth physiology. Please see next section for small microfluidic implants.

6.2d: Active Drug Delivery Control through Flexible Polymer Microneedles

- Use the new small and flexible drug delivery devices as early pupal stage implants: Use active drug delivery device for medical trials. One interesting application which may find use of this system is tightly localized of delivery for brain cancer treatment [13].

6.3 Important Lessons From My Research and a New Outlook

One of the biggest challenges I faced in my research was devising the nanoscale version of the electroactive wells. In making the 200 nm wide and 1 μm tall hollow cylinders, I spent an entire year revising different fabrication strategies that not only were tricky, but ultimately needed to follow clean room guidelines. Given that the bottom conducting electrode (ITO) is not considered a clean material since it has a very low vapor pressure and when subjected to a vacuum, it can easily diffuse into the various clean room processing chambers and contaminate them, the challenge proved even greater. So while in this lapse of my graduate career I managed to become proficient in most of the clean room tools, on hindsight, I believe that this was not the optimal way to fabricate the nanowells; at least for proof of concept experiments. I would now make the dielectric (material surrounding the hollow cylinders) using a commercially available aluminum oxide membrane made by Whatman Ltd. [14], which consists of a highly uniform array of insulation and tall hollow cylinders which match my device dimensions and can be readily purchased. Though the alumina membranes may need additional polishing in order to be thin enough for this application, this could have proven a key point in my graduate studies to think outside the box and integrate traditional nanofabrication mechanisms with alternative nanoscale processing techniques. While it may have been a missed opportunity, I made sure to look beyond the traditionally established microfabrication techniques for the subsequent drug delivery projects I engaged in by fusing multiple forms of fabrication, including 3-D printing, laser micromachining and standard clean room techniques. This proved a valuable lesson in using all the resources you have at hand as a researcher, and to understand that there are multiple ways to get to an answer but the key aspect is identifying the best means to get to it.

Another key lesson I learned stems from my work in the insect cyborg project, effective tissue re-adaptation happens for dimensions on the order of 100μm in size. In my research, this manifested itself by the fact that even though moths endured the implantation procedure, when the pupae released their cuticle (shell) during emergence, the cuticles can get stuck on the chip and prevent the insect from releasing its wings, in contrast to the other HI-MEMS [12] groups engaged in using thin electronics who do not usually see this undesired effect. The main problem here is that the microfluidic chip is large in size (~on the order of 2mm by 1mm) mainly due to the fluidic loading process, which as mentioned in Chapters 4 and 5 uses a syringe needle to fill up the drug delivery chambers. This is an interesting engineering limitation with important implications, and I would be very interested in researching wetting and sealing methods applicable in the micro and mesoscales scale to overcome this problem. The second lesson I learned (which may seem very obvious on hindsight) is that once the final product is in place, it is very hard to change its intended operation. For example, my drug delivery component works on a burst valve process, and as such it cannot become a controlled and continuous drug delivery mechanism overnight; which are key components that the drug delivery community actively seeks. Also, you cannot avoid gas bubbles in an electrolytic pump unless you use more than one chamber or use multiple drug delivery materials (say mediating the release via insulating and biocompatible silicon oil) which inevitably sacrifice chip space. Most importantly, I learned that one does not always know the pros and cons of your work *a priori*, and as such one must pay extra careful attention in the design stage. However, I would like to state that the drug delivery systems device did manage to accomplish what they were meant to do, (namely to paralyze a moth in mid-air and to present a flexible alternative to silicon drug delivery systems) but unfortunately face issues in extending the realm of applications of this work.

6.4 Concluding Remarks

I believe my work has helped expand the scope of microfluidics and provided practical solutions for its two greatest challenges: The fundamental transport limitations associated with downscaling fluid flows and the integration issues that have kept most microfluidic devices from becoming commercially viable. My hope is that other researchers will make use of my device and integrate it with their own setups without too much trouble.

REFERENCES

1. Rettig, J.R. and A. Folch, *Large-scale single-cell trapping and imaging using microwell arrays.* Analytical Chemistry, 2005. **77**(17): p. 5628-5634.
2. Blu-raydisc.com. *Blu-ray Disc Public Specs*. 2010 [Available from: http://www.blu-raydisc.com/en/Industry/Specifications/PublicSpecs.html.
3. www.gamida-cell.com. *Gamida Cell Therapy Technologies Inc.* 2010.
4. K'Owino, I.O. and O.A. Sadik, *Impedance spectroscopy: A powerful tool for rapid biomolecular screening and cell culture monitoring.* Electroanalysis, 2005. **17**(23): p. 2101-2113.
5. Huh, Y.S., A.J. Chung, B. Cordovez, and D. Erickson, *Enhanced on-chip SERS based biomolecular detection using electrokinetically active microwells.* Lab on a Chip, 2009. **9**(3): p. 433-439.
6. Cao, Y.C., R. Jin, and C.A. Mirkin, *Nanoparticles with Raman Spectroscopic Fingerprints for DNA and RNA Detection.* Science, 2002. **297**(5586): p. 1536-1540.
7. Etchegoin, P., R.C. Maher, L.F. Cohen, H. Hartigan, R.J.C. Brown, M.J.T. Milton, and J.C. Gallop, *New limits in ultrasensitive trace detection by surface enhanced Raman scattering (SERS).* Chemical Physics Letters, 2003. **375**(1-2): p. 84-90.
8. Yin, Y. and A.P. Alivisatos, *Colloidal nanocrystal synthesis and the organic-inorganic interface.* Nature, 2005. **437**(7059): p. 664-670.
9. Venter, J.C., M.D. Adams, E.W. Myers, P.W. Li, R.J. Mural, G.G. Sutton, et al., *The Sequence of the Human Genome.* Science, 2001. **291**(5507): p. 1304-1351.

10. Claassen, D.E. and A.E. Kammer, *Effects of Octopamine, Dopamine, and Serotonin on Production of Flight Motor Output by Thoracic Ganglia of Manduca-Sexta.* Journal of Neurobiology, 1986. **17**(1): p. 1-14.
11. Johnston, R.M. and R.B. Levine, *Crawling motor patterns induced by pilocarpine in isolated larval nerve cords of Manduca sexta.* Journal of Neurophysiology, 1996. **76(**5): p. 3178-3195.
12. Judy, P.M.J. *Hybrid Insect MEMS.* 2010 [Available from: http://www.darpa.mil/mto/programs/himems/index.html.
13. Gallia, G.L., S. Brem, and H. Brem, *Local treatment of malignant brain tumors using implantable chemotherapeutic polymers.* J Natl Compr Canc Netw, 2005. **3(**5): p. 721-8.
14. http://www.whatman.com/PRODAnoporeInorganicMembranes.aspx. *Whatman LTD.* 2010.